# DEVELOPMENT AND CHARACTERIZATION OF A DROPLET-BASED MATERIAL FEED SYSTEM FOR MULTI-MATERIAL PROJECTION MICRO-STEREOLITHOGRAPHY

By

JAY TOBIA

A thesis submitted to the

Graduate School-New Brunswick

Rutgers, The State University of New Jersey

In partial fulfillment of the requirements

For the degree of

Master of Science

Graduate Program in Mechanical and Aerospace Engineering

Written under the direction of

Howon Lee

And approved by

_____

_____

_____

New Brunswick, New Jersey

May 2016

ABSTRACT OF THE THESIS

Development and Characterization of a Droplet-Based Material Feed System for Multi-Material Projection Micro-Stereolithography

by Jay Tobia

Thesis Director:

Howon Lee

Current additive manufacturing techniques focus on creating useful three dimensional (3D) objects from a single material. The inability to incorporate multiple materials in a single part limits the ability of additive manufacturing technology to create objects with engineered properties and functions. This research aims to develop a process by which multiple materials can be integrated into a single object in a fast, efficient, and scalable operation. A droplet-based material feed system for projection micro-stereolithography solves current problems with 3D printing of multiple materials by allowing printing materials to be switched by depositing droplets of different liquid resins. Precise control of small droplet volume is obtained by pressure control of the resin injection nozzles, exact opening times of fluid valves, and appropriate surface coatings in order to portion droplets so that just enough material is brought to the build area, resulting in minimal material waste. Digitally modulated high resolution light patterns solidifies thin layers of ultraviolet curable resin in succession to build a final 3D object in a layer by layer fashion. The effectiveness of this novel solution is discussed by creating

objects similar to those of other systems and measuring total build time, material waste, and final print quality. The ability of the process to be scaled up allows for printing of high resolution multi-material objects on a large scale. The multi-material additive manufacturing technique with efficient materials management will enable the cost effective and rapid production of new engineering applications such as bio-inspired soft robotics, biomedical micro-devices, and functional tissue scaffolds.

# ACKNOWLEDGEMENTS

I would like to thank my advisor, Dr. Howon Lee, for his continuous support, guidance, and support during the entirety of my research. His support and direction has helped me immensely in the research process.

I would also like to thank the rest of my thesis committee, Dr. Aaron Mazzeo and Dr. Shahab Shojaei-Zadeh for their willingness to join my thesis committee and the time that they took out of their schedules to review my thesis.

A lot of thanks also goes to my lab mates. Chen Yang, Daehoon Han, Lucas Lu, and Woojin Chae have been great to work with and have helped me at various points throughout my research. A large thanks also goes to Jason Kim, who worked on performing the curing depth studies that are included in this thesis.

Most importantly, I would like to thank my family for their constant support throughout my college education. My parents and grandparents have been amazingly supportive throughout this whole process, and I would not be able to have completed my college education without their help.

TABLE OF CONTENTS

LIST OF TABLES

LIST OF ILLUSTRATIONS

# 1 Introduction

## 1.1 Background

Recently, additive manufacturing, also often referred to as 3D printing has been a popular topic of discussion in the mainstream media. The ability for users to build a physical 3D model directly from a 3D part drawing allows for an ease of use that was previously unobtainable. Arguably more interesting is the ability to construct objects that were impossible to build using typical subtractive machining methods such as drilling, cutting machining, etc. This flexibility of design allows for new objects to be designed in ways that were previously impossible.

3D printers have developed in many different sizes. On the large end of the scale, there are 3D printers being developed that are being used to build concrete houses [1]. On the small end of the scale, the Nanoscribe 3D printer has the finest resolution of any commercially available 3D printer. This printer makes objects ranging in sizes from a few microns in size up to a few millimeters, and feature sizes reach down to sub-micron levels [4]. In between are the most popular 3D printers. These 3D printers can construct objects by extruding a thermoplastic from an extruder [2], or by curing a liquid resin [4] [12]. These 3D printers are used for rapid prototyping of parts and for sometimes for production parts. Typically, these 3D printers build objects from a single material, which is suitable for prototyping or other simple needs. In order for 3D printing technology to advance, it is important that 3D printers can incorporate multiple materials into a single part. Multiple materials expand design possibilities for example by allowing parts to be

flexible in one area and rigid in another or to contain a drug in one area but a slow dissolving material in another area.

Possibly the most popular form of multiple material 3D printing is the fused deposition modeling (FDM) method. Many current consumer level 3D printers use this technology for its ease of use and inexpensive material and system cost. FDM printers work by heating and extruding a thermoplastic through a nozzle. The nozzle traces the 2D layer of the object that is to be build, before moving up the next layer. Multiple material FDM have been developed so that multiple colors or types of material can be combined into one part. D. Espalin *et al.* have developed a multiple material FDM printed that has two separate printing areas, one for each material. The print bed cycles between these two printing areas to print the different materials [5]. Other companies, such as Makerbot, simply use multiple extruders in their FDM printers. Each extruder holds a separate material, and after one nozzle prints one layer, the second nozzle fills in where the second material should be. FDM printers are advantageous because of their low cost and good performance, however because they extrude plastic through a small nozzle, they are not able to replicate very small parts or fine structures. One of the most popular consumer grade multi-material FDM printers is the Makerbot Replicator 2x. This printer is capable of a layer height of 100 microns, which is typical of similar models produced by other companies. The resolution of features is limited by the size of the nozzle, which is 0.4mm in diameter for the Replicator 2x [6]. A more production geared 3D printer is the Dimension Elite 3D printer by Stratasys. Surprisingly, this printer has a minimum layer height of 178 microns, thicker than that of the Makerbot. Stratasys does not publish the

dimension of the nozzle inner diameter. A thicker layer thickness will allow the Dimension Elite to print in less time, possibly the reason of the thicker printing thickness [2]. All materials used in a FDM printing system must be thermoplastics, so that they can be melted and extruded through the printing nozzle, limiting the materials that can be printed by the system.

Similar to FDM printers, multi-material bio printers push material out of fine nozzles in order to create a final part. Unlike FDM printers, the entire part is cured after printing with UV light that activates a cross linker in the printed material. This method of printing is commonly used in biological research, since the process is gentle on the printed cells. 3D bio printing is becoming so popular because of the ability to print a three dimensional scaffold where cells can be grown. In the body, cells are always close to a supply of nutrients, and the same supply of nutrients and oxygen must be supplied to cells in the lab [7]. Lewis *et al.* have been successful in using a multiple material nozzle based printer to print three dimensional cell-laden tissue. A multi-material printer allows for multiple types of cells to be printed, as well as inks that can be washed away after printing in order to provide vasculature with which the cells can be fed [8]. They have also used a similar printer, also a nozzle based, to print biomimetic 4D structures. The nozzle aligns cellulose fibers in the printed material, that cause anisotropic swelling in the final printed part. By printing objects in a predetermined path, the final printed objects will swell predictably when placed in water, allowing the originally flat printed shapes to swell and curl, closely mimicking the botanical systems that the part was modeled after [9].

Another technology for multi-material 3D printing is polyjet 3D printing. Like the name suggests, polyjet printers use inkjet technology to drop fine drops of UV curable resin, that are then cured by a UV light that travels with the print head. One common polyjet 3D printer is the Objet30 pro. This machine can print layer thicknesses down to 28 microns thick and has a resolution of 600 dpi, or 42.3 nanometers per droplet [10]. This resolution far surpasses that of FDM printers, but the system is not without its drawbacks. Commercial polyjet 3D printers must use the vendor supplied materials, which limits the flexibility of the system. The Palo Alto Research Center has developed their own multi-material polyjet 3D printers using an inkjet print head. They have been able to print UV and thermally curable materials from their system such as UV gel inks and sacrificial support material, but have not released any more information about the range of materials that they are able to print [11]. Ultimately, polyjet printers are will not be able to print materials with very high viscosities or with particle suspensions, as these materials will not pass through the ink jet print heads.

Projection micro-stereolithography (PμSL) is a system originally developed to replace silicon micromachining technology. By using a digital dynamic mask, such as the ones found inside standard video projectors, patterned light can be focused to a very small area to fabricate parts with micron sized features. The dynamic digital mask is able to project light using any combination of its pixels, allowing for a 2D image to be projected. This allows an entire 2D image to be cured in one process. Competing systems, like stereolithography, use a scanning laser that must scan the entire 2D image that is to be printed. PμSL systems cut down considerably on build time compared to competing

technologies, and are still able to resolve micron sized features [12] [13]. The ability of the PμSL system can be used to print many objects using a patterning technique. After one 2D image is displayed, the stage simply moves on the x and y axes, and a new 2D image is projected. Using this method, arrays of high resolution parts can be printed in ashort amount of time [14]. While PμSL systems display a lot of benefits as a 3D printing system, a method for multiple material printing must be explored to make full use of the technology.

One way to add multiple material capability to a liquid resin based 3D printing system is to use multiple resin baths. Wicker *et al* have used this method with success. In this particular system, one material of the part is fully constructed before the object is cleaned and brought to the next material. This method shortens built time of the total process, but is unable to construct very complex multiple material parts. This is because if one material is sandwiched in between another type of material, the system cannot print one material all at once and then the other, it must print them in order, eliminating the time savings that the system aimed to save [15]. A similar method of multiple material 3D printing using multiple resin baths has been developed at the University of Southern California. This system also uses multiple resin baths to create a multiple material part. In this system, the part is cleaned and switched between resin baths for each successive layer. The cleaning process used in this system is quite harsh on the printed parts, and so fine features (< 0.3mm) cannot be printed without being broken by the cleaning process. The cleaning process is necessary to reduce material bleed over. Material bleed over occurs when some resin remains on the printed part when it is transferred to the next resin. This leftover resin will cure with the new resin, making an imperfect structure [16].

Both of these systems suffer from long build time for complex multiple material parts, and difficulty in printing fine resolution parts due to issues with the leveling of the resin baths and with the cleaning methods used.

A much more suitable method for constructing multiple material objects from a liquid resin is the refillable chamber system. In this type of system, a chamber is filled with a liquid resin, that resin is cured, and then the remaining liquid resin is flushed out with the second resin. This process is explained in FIGURE 1.1.

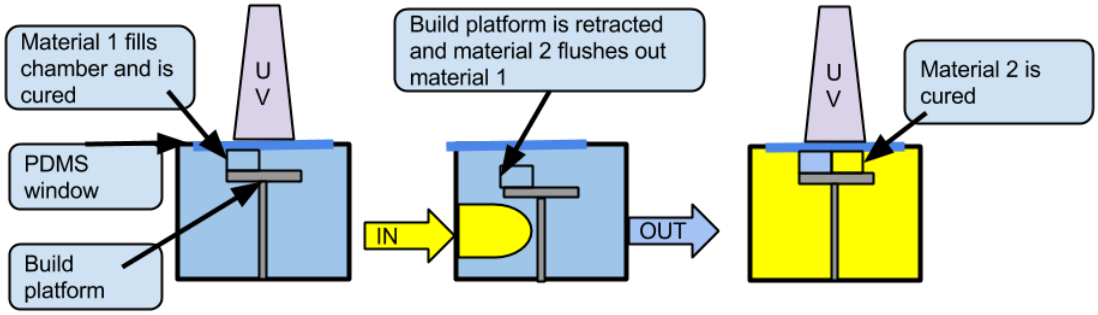


**FIGURE 1.1: Process diagram for multiple material chamber system**

This chamber system provides benefits for constructing fine featured parts compared to the rotating vat system. In the chamber system, the part does not need to move around, and harsh cleaning methods are not used to remove excess resin. The flow of new resin is able to flush away old resin, putting minimal stress on the part, but also wasting lots of material. This flushing process wastes a lot of material, especially if materials are switched between often [17].

The large amount of material waste created by the multiple material chamber system is a large problem, especially when printing objects made of expensive materials, such as specific biomaterials. Current methods for printing multiple material parts from liquid resin all contain some sort of drawback. The polyjet process is able to achieve very fine resolution and fast build times, but only works with materials in a certain viscosity that do not have any particle suspensions. The rotating vat system is unsuitable for fine structures because of the long build times and harsh cleaning methods used. Furthermore, large amounts of resin are needed to fill up the vats in the first place, which can cause a problem when working with expensive materials. Finally, the chamber system is suitable for fine structures, but makes a large amount of material waste during the printing process. In order to address these issues with current printing systems, a new type of multiple material printing method must be devised.

| | Multiple Material Printing Technology | | | | |
|---|---|---|---|---|---|
| | Fused Deposition | Polyjet | Resin Bath | Chamber | Nozzle |
| High Resolution | □ | ○ | ○ | ○ | □ |
| Material Flexibility | ◊ | ◊ | ○ | ○ | ○ |
| High Part Strength | ○ | ○ | ○ | ○ | □ |
| Suitable for bio materials | □ | ◊ | ◊ | ◊ | ○ |
| Low Material Waste | ○ | ○ | ○ | □ | ○ |
| | □ = poor, ◊ = acceptable, ○= good | | | | |

**TABLE 1.1: Review of multiple material 3D printing technologies**

## 1.2 Motivation

The objective of this research is to develop a multi-material 3D printer capable of printing objects with micron resolution and minimal material waste. These requirements are not currently met in any currently existing 3D printing system. Drawbacks of current multiple material 3D printing systems reduce their usefulness and are holding back the adoption of multiple material 3D printing technology.

In order to achieve a fine resolution of the printed object and fast build times, a digital mask based projection system will be used. This system can be used for many different size parts depending on the optics used. This system will use reduction optics coupled with a digital mask based projection system to print small objects (~8mm x ~6mm area) with fine features (<50 μm).

When printing objects with fine features, great care must be taken in order to ensure that these features are not broken during the printing process. Some printing systems use harsh cleaning methods in order to reduce material bleed over during the printing process [15]. In order to ensure a perfectly intact printed object cleaning will be performed without the aid of mechanical removal of material or other harsh processes.

The system must also have minimal material bleed over when incorporating multiple materials in one final part. A large amount of cross contamination between the two materials will defeat the purpose of a multiple material system. The final parts must display a clear delineation between the different materials used. While minimizing material bleed over, material usage must be minimized. Many materials, especially those in the biomedical field, are very expensive. Excessive waste of these materials will

increase costs of the printed part dramatically and will limit the usability of the multiple material 3D printing system. Possible the most important feature of the droplet based multiple material 3D printer is the minimal usage of material.

Finally, the developed system should ideally work with a multitude of materials. Since this system will utilize UV curing of materials, any material that is curable with UV light should be able to be used in the system. Other systems contain valves or rely on flow of material through a chamber in order to print. These systems will not work well for very viscous materials or for materials with high concentrations of suspended particles. The droplet based printing system will be able to work with very viscous materials, and materials with high concentrations of suspended particles. Unlike other systems, liquids larger particles suspended in them can be printed, since the particles that fall to the bottom of the liquid will still be cured, while they will fall out of the build area in other systems.

A multiple material 3D printing system with minimal material waste, ability to print fine structure, and scalability to different materials, especially traditionally difficult to print materials, will be a significant improvement to existing systems. The goal of this research is to develop a 3D printing system capable of meeting all of these criteria in order to increase the usability and utility of the multi-material 3D printer.

# 2 System and Characterization

This section will describe the operation and design of the droplet based multiple-material 3D printer in addition to quantifying its performance. Example prints from the system will be shown, and material waste will be compared to competing multiple-material 3D printers. The results from this section will allow readers to understand the operation and advantages of this system.

## 2.1 System description

In order to understand the droplet based multiple-material 3D printer, the individual systems that make up the printer must be understood. There are three main parts of the system, as shown in FIGURE 2.1. The first is the projection system, which consists of a UV light projector and reduction optics. This projector uses a dynamic mask to display a 2D image that will cure the resin in that exact shape.

The next portion of the system is the Z axis stage and the rotating build platform. The Z axis stage holds the printed part and moves it up and down during the printing process. The rotating platform moves the resin droplets from the material deposition system to the area where the resin is cured. This rotating platform is transparent to let the patterned light through and non-stick to prevent the printed part from sticking.

The final portion of the system is the material droplet system. This system uses air pressure to extract exact amounts of resin onto the rotating build platform. The nozzles move up and down with the material droplet stage to prevent the nozzles from interfering

with droplets of resin. The pinch valves are used to control the amount of each resin that is extracted.

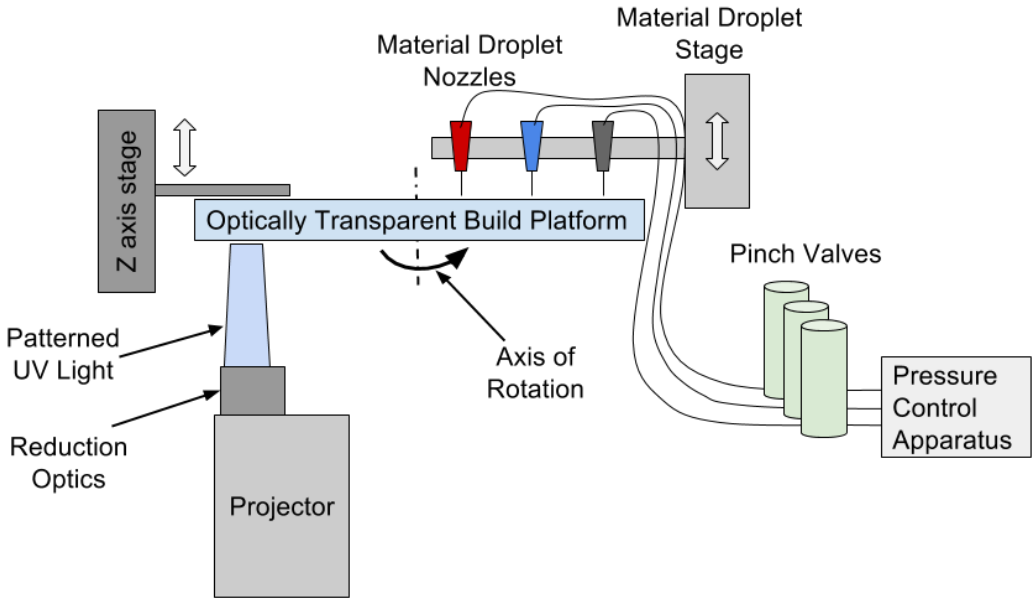


**FIGURE 2.1: System diagram of the droplet based multiple-material 3D printer**

### 2.1.1 Printing process description

The printing process must be controlled in order to make sure that the part is built correctly. 3D printing is a layer by layer process, so understanding the process that the system uses to complete one layer of the object will allow the entire process to be understood. FIGURE 2.2 explains the printing process for a single layer of the printed part.

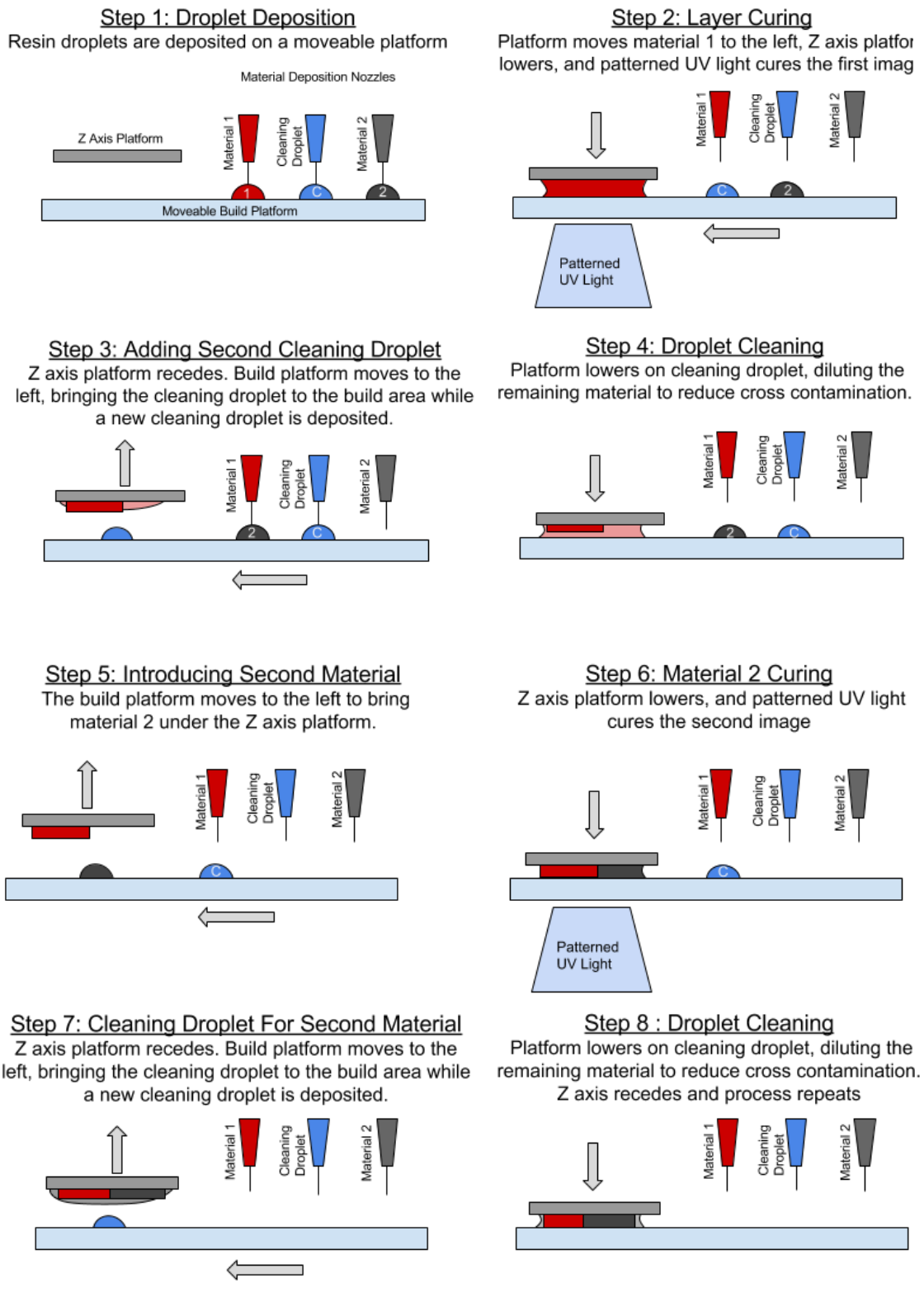


**FIGURE 2.2: Printing process of the droplet based multiple-material 3D printer**

For step 1 of the printing process, the liquid resin droplets are placed on the moveable build platform. After those droplets are placed, the nozzles recede and the platform rotates to bring the first resin droplet to the build area. In step 2, and Z axis platform lowers to the height of the first layer, and the resin is cured by the projector. After the resin is cured. The Z axis recedes, leaving some of the leftover resin on the platform and some of the resin stays with the printed part. Next, in step 3, the cleaning droplet (ethanol) is brought over to the build area. The material deposition nozzles also lower at this time, to lay down another cleaning droplet. In step 4, the Z axis lowers again, but this time to clean the part. The ethanol dilutes the remaining material on the part, reducing material bleed over.

Now, in step 5, the second material is brought to the build area so that it may be printed alongside the first material. In step 6 the Z axis lowers to the same distance that it did for the first material. A different pattern of light from the projector cures the second material alongside the first. As before, there is still uncured material still left on the printed part. The moveable build platform moves the remaining cleaning droplet over to the build area in step 7. In the last step, step 8, the Z axis lowers again to let the cleaning droplet draw away the remaining resin. The Z axis then recedes, and the process can begin again. All of the layers of the part are constructed using this same process. By stacking layers upon layers of cured resin, a 3D part is created.

### 2.1.2 Mechanical principles of the system

The mechanical design of the 3D printing system is very important for the operation of the printer and will determine the quality of the final printed object. The 3D printing system has a few main mechanical systems that are shown in FIGURE 2.3. The Z axis stage moves the printed object up and down using a linear stage. A gear attached to a stepper motor rotates the clear build platform that moves the resin droplets to the build area. The resin droplet system consists of a stage that moves the nozzles, pinch valves to control the flow of the resin, and the tubing and nozzles.

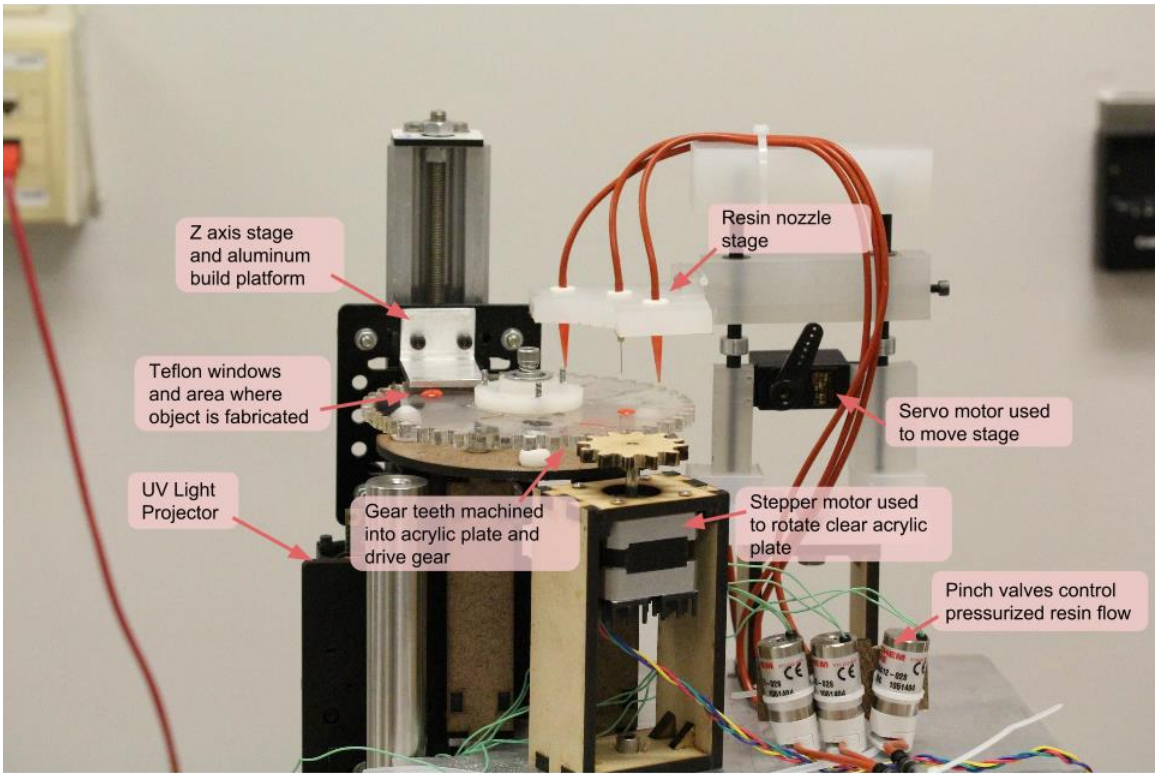


**FIGURE 2.3: Mechanical design of the 3D printing system**

### 2.1.3 Rotating build platform

The rotational platform has three key design criteria. First, the rotational platform must be coated in such a way that the cured resin will not stick to it. This is to ensure that the layers of the object stick to the previous layer and are not carried away with the rotational platform. Second, the rotational platform must be able to rotate a set amount of degrees accurately so that the resin droplets are brought to exactly to the right spot each and every time. Finally, the rotational platform must maintain a consistent height in the build area. If the plate wobbles up and down, the layers will not be consistent thicknesses, they will vary in thickness as the platform rotates.

The build platform's only motion is rotation. The platform is made of ¼ inch thick acrylic, and has a gear pattern laser cut around the circumference. The gear pattern allows a laser cut gear constructed of MDF (medium density fiberboard) that is connected to a stepper motor, to rotate the platform. The platform rotates around a central axis, which is constructed from a ¼-20 bolt. The platform has a machined polypropylene piece that holds a rotational bearing securely to the center of the platform. The ¼-20 bolt is run through this bearing, providing a solid axis of rotation.

In order to keep the cured resin from sticking to the acrylic platform, adhesive backed Teflon tape is stuck to the acrylic plate. The minimal friction from the Teflon allows the cured layers to easily separate from the platform

The build platform must maintain a consistent height throughout its full rotation in order to ensure that the layers of the object are all equal heights. In order to achieve this design criteria, the rotation and support of the platform were decoupled. This means that the

mechanism that allows the platform to rotate does not also support the platform. This system is shown in FIGURE 2.4. To support the platform, a set of Delrin balls are used. These four Delrin balls sit at equal heights in a laser cut MDF piece. The rotational platform sits on top of these Delrin balls which provide minimal friction for easy rotation. In order to press down the rotational platform against the balls, a spring is placed between the bolt of the rotational platform and the top of the rotational bearing. This places downward force on the platform, ensuring that the position of the rotational platform does not shift. The rotational bearing is held in a piece machined from polypropylene, which is bolted onto the rotational platform.

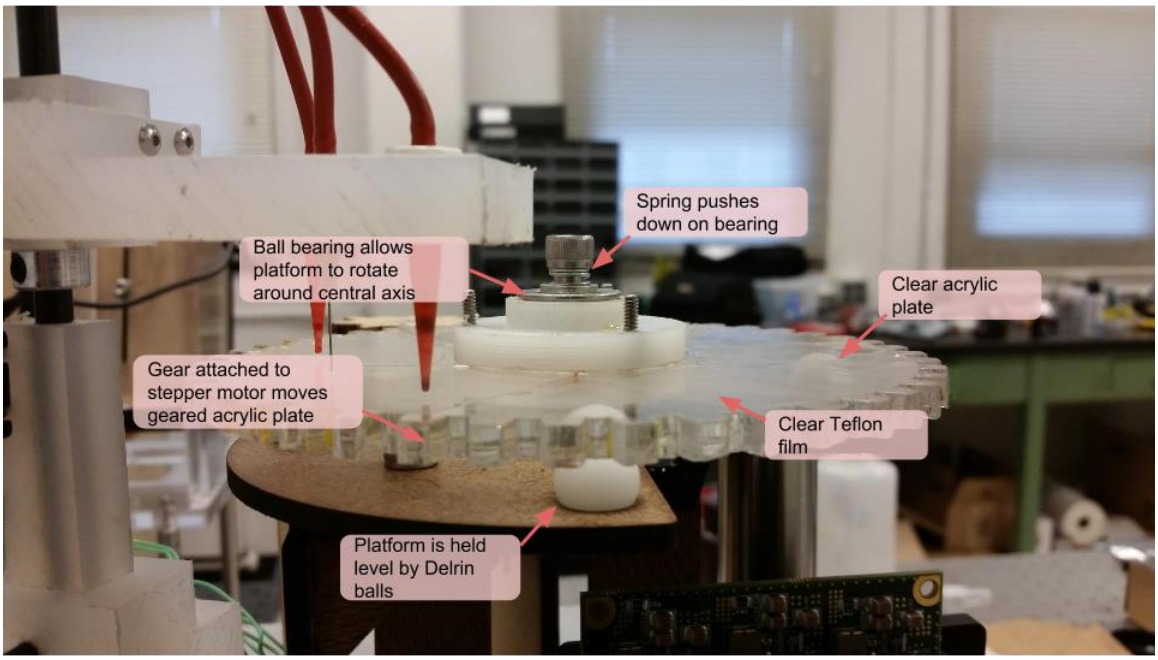


**FIGURE 2.4: Mechanical design of the rotating build platform**

The run out of the rotational platform was measured to ensure that the height variation over the rotation of the platform was not significant. The run out is the difference in height between the lowest spot and the highest spot on the platform. To test this, a dial indicator was held against the rotating platform. The height of the platform was measured every 30 degrees of rotation for three rotations (TEST 1, 2, and 3). The results of the testing are shown in TABLE 2.1. The largest run out measured over one rotation was 14µm. This means that over the course of 2 printed layers, the height difference will be approximately 14µm or 7µm per layer. Since the layer heights are approximately 50 to 100µm, this level of run out is acceptable.

| | TEST 1 | TEST 2 | TEST 3 |
|---|---|---|---|
| height reading at 0° rotation | 57.2 | 62.2 | 62.2 |
| height reading at 60° rotation | 62.2 | 69.9 | 69.9 |
| height reading at 120° rotation | 61.0 | 63.5 | 61.0 |
| height reading at 180° rotation | 69.9 | 57.2 | 57.2 |
| height reading at 240° rotation | 62.2 | 59.7 | 61.0 |
| height reading at 300° rotation | 55.9 | 64.8 | 62.2 |
| **Run Out (µm)** | **14.0** | **12.7** | **12.7** |

**TABLE 2.1: Run out testing for the rotating platform**

### 2.1.4 Pressure control system

The pressure that each resin is held under must be different, according to the viscosity of the resin. A higher viscosity resin will need more pressure to force the resin through the tubing. In order to achieve multiple pressures without using multiple pressure regulators, a pressure control system was setup as shown in FIGURE 2.5.

High pressure enters the omega pressure regulator, and is then regulated down to a low pressure (around 2psi) for use in the pressure control system. These is one branch for each of the material droplet nozzles, three in this case. For each branch, there is a pressure gauge, a T- barbed fitting, and needle valve. Each branch receives the same pressure from the pressure regulator. If the needle valve is fully closed, then the pressure that is placed on the resin will be the same pressure that the pressure regulator outputs. As the needle valves are opened, the pressure in the branch drops, lowering the pressure on the resin. The pressure gauges on each branch show the individual pressures for each branch. The system is effective at supplying different pressures to each resin, enabling the droplet extraction to be precisely controlled.

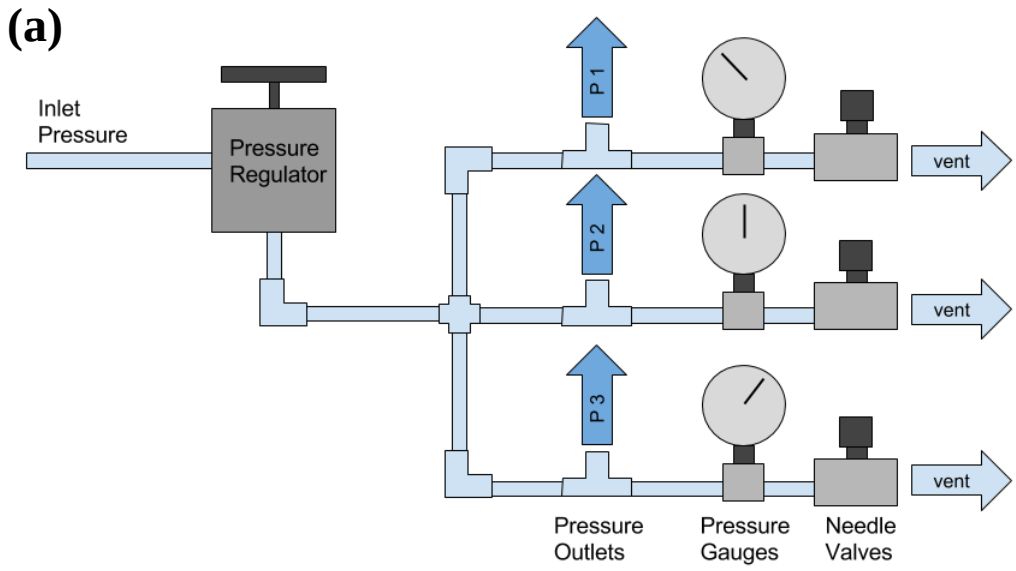

**(b)**

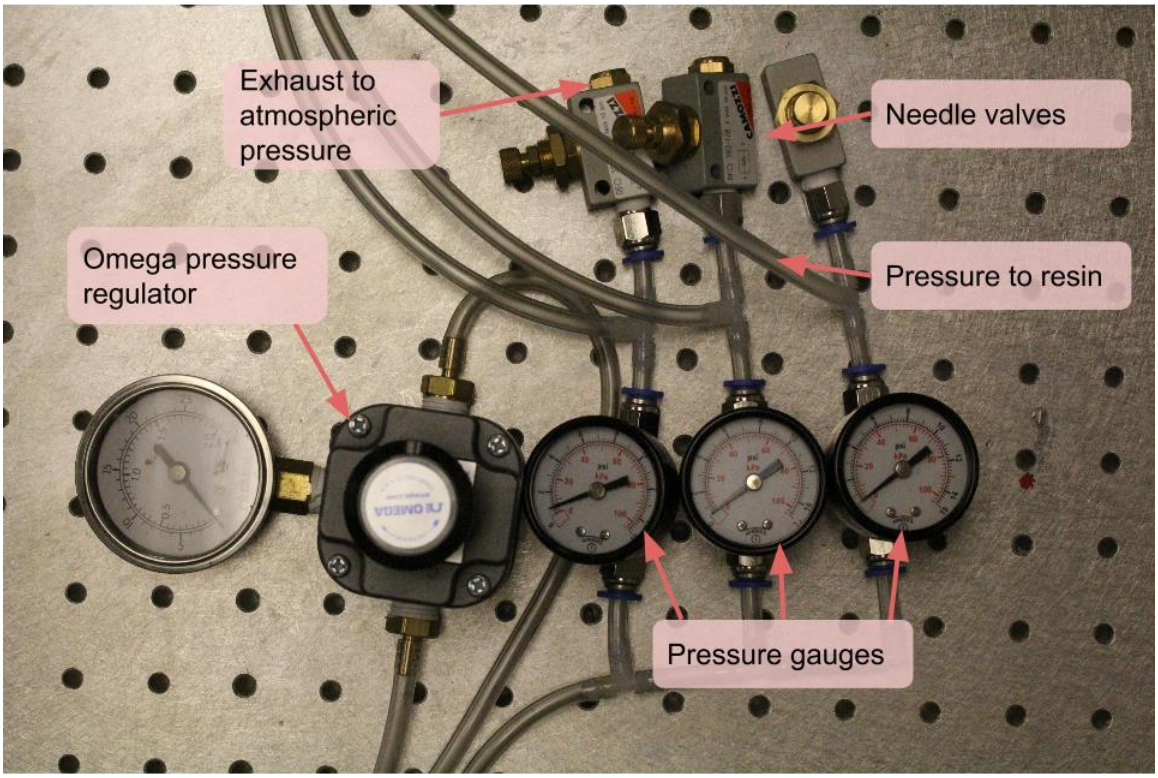


**FIGURE 2.5: Pressure control system (a) diagram for the layout of the system (b) photo of the full pressure control system**

### 2.1.5 Electronics of the system

The electronics of the system control the movement of every mechanical component of the system. The electronics must control the z axis, pinch valves, rotational platform stepper motor, and the nozzle stage servo motor. To send all the commands for all of these separate pieces, an Arduino microcontroller is used. The Arduino directly controls the servo motor, sends signals to the power electronics that open the pinch valves, and sends signals to the stepper motor controllers that control the rotation of both stepper

motors. The whole electronics layout and wiring of the electronics is shown in FIGURE 2.6.

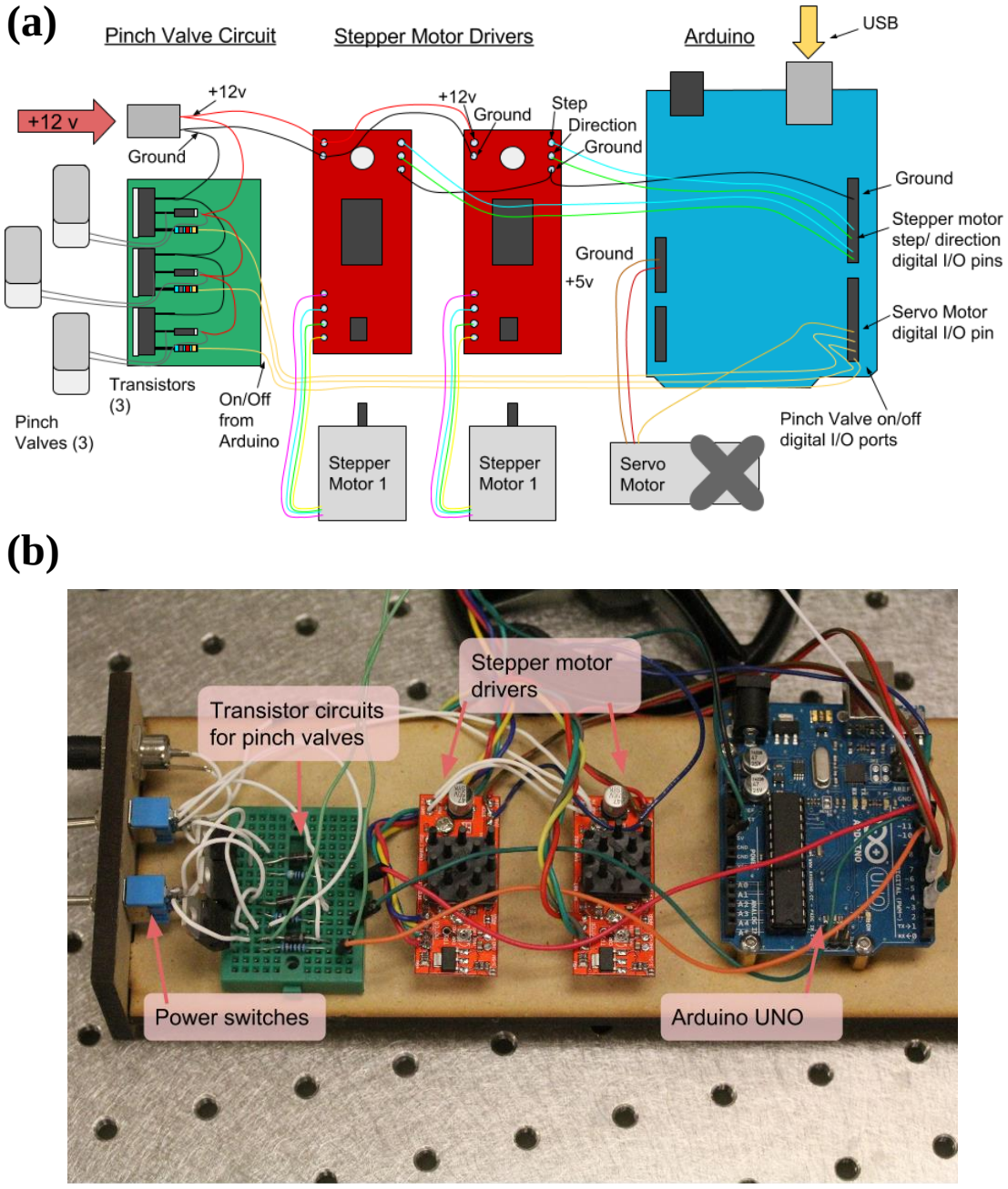


**FIGURE 2.6: Electronics for the printing system (a) layout diagram for the wiring of the electronics (b) photo of the electronics components**

The stepper motors draw too much current to be driven directly by the Arduino. The Arduino can only supply a maximum voltage of 5V at 20mA, and the stepper motor requires a peak of 350mA at 12V. In order to control the stepper motors, an EasyDriver Stepper Motor Driver was used, which is based around the A3967 Microstepping Driver made by Allegro. The EasyDriver takes the 12V input voltage, and translates it into the correct pulses to move the stepper motor, based on the digital 5V signal sent from the Arduino. This board can supply a peak power of 700mA at 12 volts, more than enough for the stepper motor.

The pinch valves, like the stepper motors, require too much voltage (12V) to be powered directly by the Arduino. The transistor circuit allows a small signal to control a large voltage. In this case, the 5V signal from the Arduino allows 12V to flow through the pinch valve opening it. The diodes in the transistor circuit are necessary when powering solenoid valves (which pinch valves are) in order to eliminate flyback, which is the reverse voltage spike caused when the voltage induces a magnetic flux in the windings of the solenoid valve. The resistors are used to limit the current drawn from the Arduino. The circuit diagram for the transistor circuit that powers all three solenoid valves is shown in FIGURE 2.7.

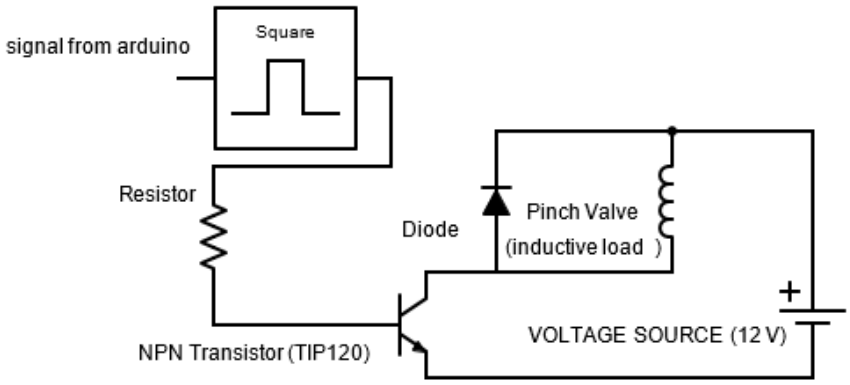


**FIGURE 2.7: Transistor circuit for pinch valve control**

### 2.1.6 Projection/ optics components

In order to project the patterned light, a CEL5500 Light Engine purchased from Digital Light Innovations (Austin, TX) was used. The system was customized with a 405nm LED light source, which is the correct wavelength that the photo initiator used in the resins responds to. The CEL5500 light engine is based around the 5500 DLP® chipset from Texas Instrument (Dallas, TX), which features the .55" XGA DMD. The DMD (digital mirror device) is the part of the system that creates the patterned light images, and is able to create better contrast than an LCD (liquid crystal display) based projector system. The projector has a resolution of 1024 x 768 pixels and can be used with a variety of lenses in order to focus the light. A plan type 5x objective lens (numerical aperture 0.13, infinity corrected) from a microscope was added to the system to reduce the size of the projected image by 5 times. FIGURE 2.8 shows the CEL 5500 projector and the reduction optics. The 405nm light originates from the UV led attached to the heatsink and fan. The light passes through a collimator, bounces off a mirror and goes

through a prism before reaching the DMD chip. The DMD chip allows the correct pixels of light to pass through the 5x reduction lens and finally to the build area where resin is cured.

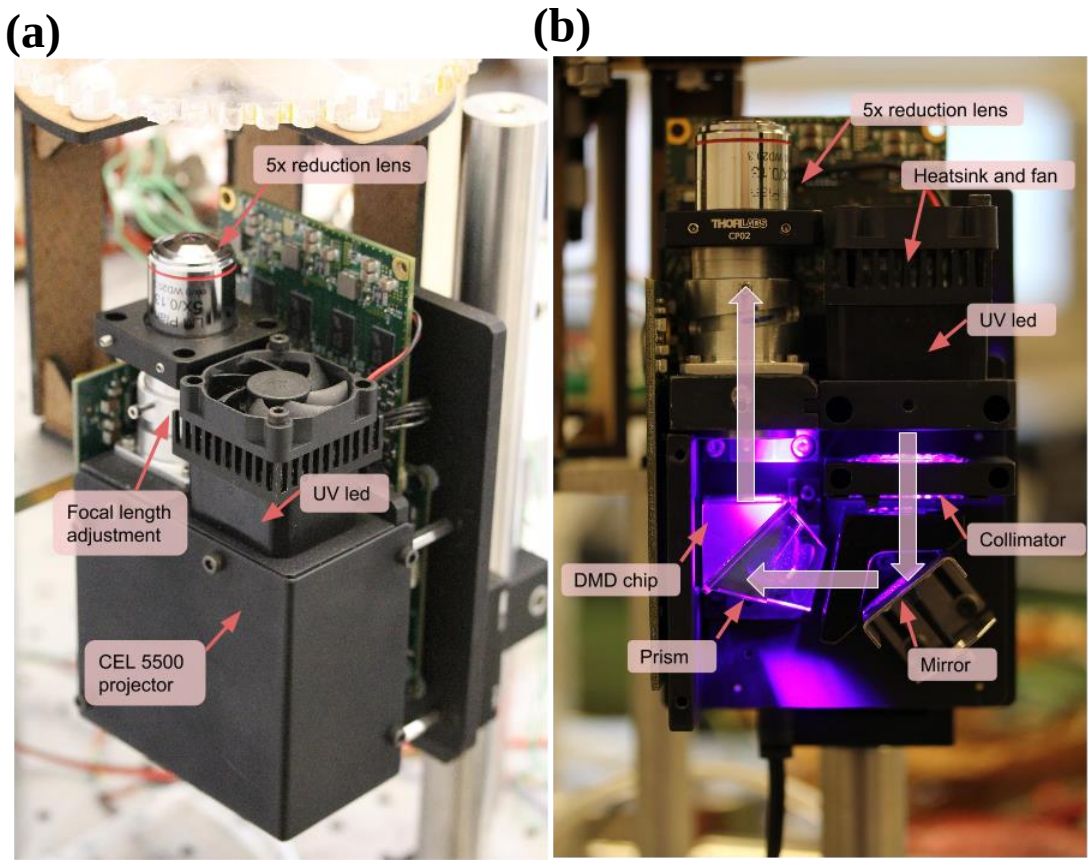


**FIGURE 2.8: CEL 5500 UV light projector (a) photo of the configuration of the projector (b) light path and internal components of the projector**

### 2.1.7 Resin chemistry

Any polymer that can be cured with UV light can be used in this printing system. The three polymers that were used in this thesis are poly(ethylene glycol) diacrylate with a molecular weight of 250 and 575 (henceforth referred to as PEGDA 250 and PEGDA 575, and 1,6-hexanedoil diacrylate (henceforth referred to as HDDA). In order to make these polymers cure in response to UV light, a photo initiator is added, specifically

phenylbis(2,4,6-trimethylbenzoyl)phosphine oxide in a concentration of 2 wt. % be weight. A photo initiator releases free radicals when exposed to the correct wavelength of UV light (405 nm in this case). Photo absorbers are also added in order to control the curing depth of the resin. The photo absorbers used in the following experiments are Sudan 1 dye (an orange colored dye), Rhodamine B dye (a pink dye that also fluoresces pink under UV light), and 3,3'-diethyloxacarbocyanine iodide (a yellow dye that fluoresces blue under UV light, and will be henceforth be referred to as $DiOC_2$). These dyes are typically used in concentrations ranging from 0.05% to 0.2% by weight. All materials were purchased from Sigma-Aldrich (St. Louis, MO) and were used without further purification.

### 2.1.8 Programming of the system

The entire printing process is controlled through LabVIEW (National Instruments, Austin, TX). The printing process described in FIGURE 2.9 is all contained in the programming of the LabVIEW code. The LabVIEW program combined with NI-IMAQ driver is able to control the image projection by accessing the UV light projector as a second monitor for the desktop PC. This allows the program to easily display the bitmap (BMP) images that will be projected. In order to control the hardware of the 3D printer, an Arduino microcontroller is used. LabVIEW sends commands to the Arduino using the LabVIEW Interface for Arduino add on for LabVIEW.

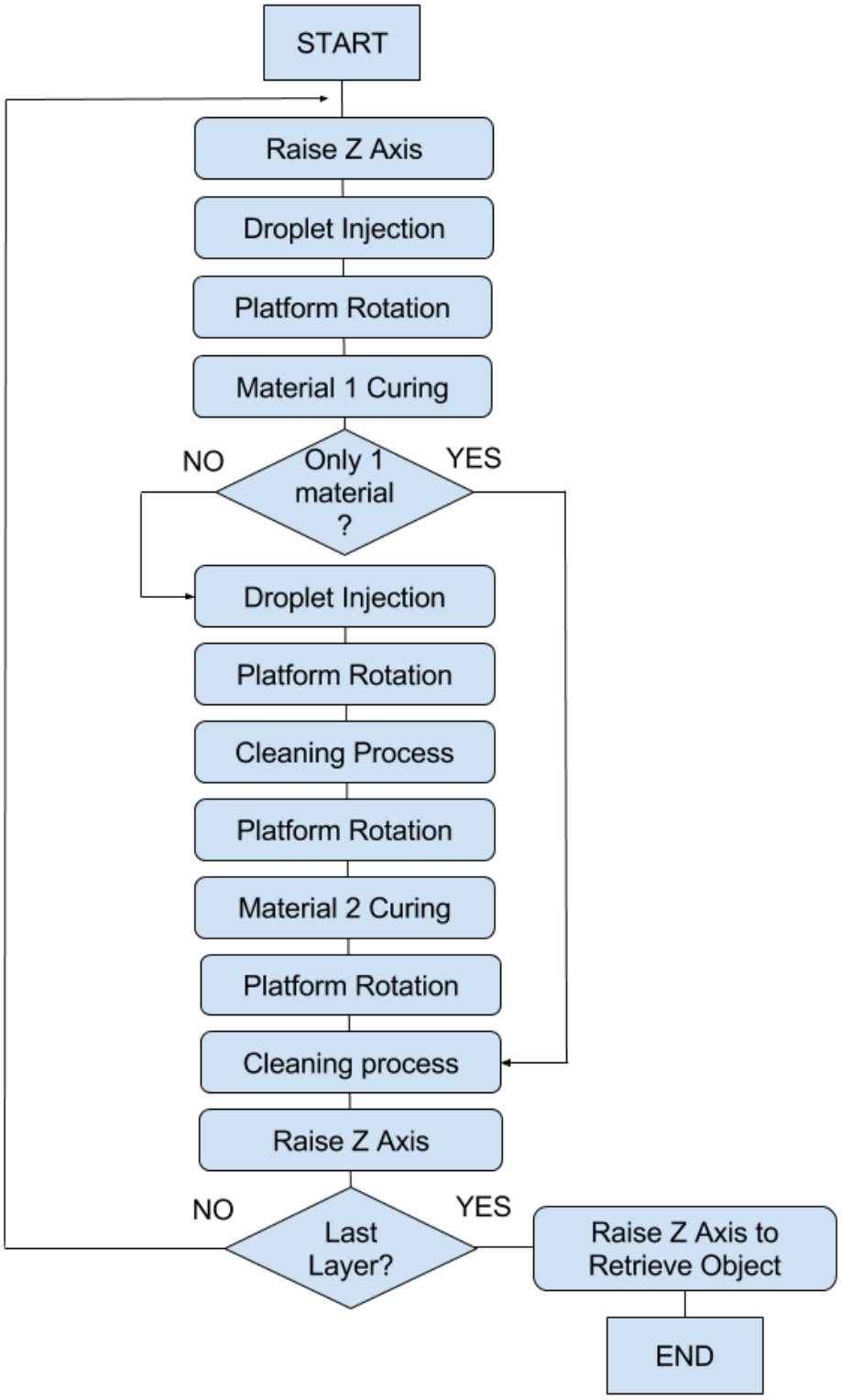


**FIGURE 2.9: Logic of the LabVIEW code**

The LabVIEW code front panel is shown in FIGURE 2.10. In order to operate the system, the exposure times for each set of image files should be set first. Different curing times can be set for each material. Next, the number of layers should be set, which is the same number of image files that are contained in either image folder. After these parameters are set, the “start print” button is pressed. This will then open a box asking for the first image folder to be opened. Select the first image in the image folder. Then, a new dialog box will open and the first image for the second material set of images should be selected. Each set of images has their own individual naming. All of the material A images will be contained in one folder and will be named like “materialA 0.bmp”, “materialA 1.bmp”, etc. After the images are selected, the program will begin running the printer. The rest of the inputs for the code, such as the valve opening time, rotation of the stepper motors, and the rotation for the servo motors are contained in the back end of the LabVIEW code, so that they cannot be accidentally changed.

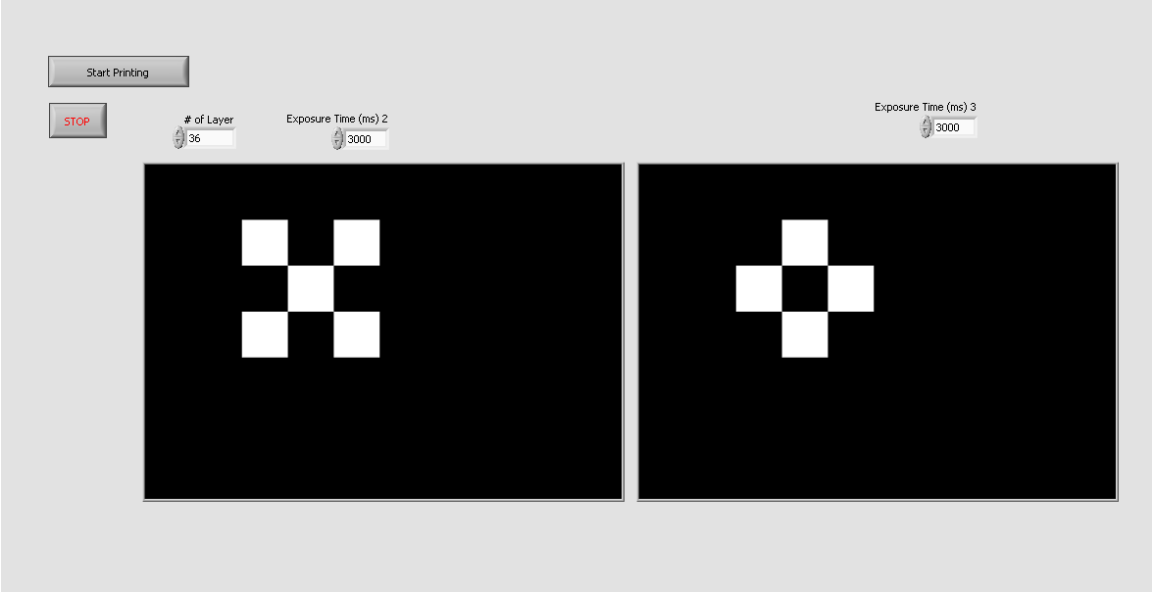


**FIGURE 2.10: LabVIEW front panel**

## 2.2 System characterization

The printing performance of the 3D printing system must be determined in order to determine what the characteristics the printed parts will have and also in order to compare this 3D printing system to other 3D printing systems. Characterization of the projector, the curing of the resin, and the multiple material performance of the system was performed in order to characterize the performance of the system.

### 2.2.1 Optics

To characterize the performance of the projector and the optics of the system, three main tests were performed. An optical resolution test was performed in order to determine the ratio between the pixel size of the image, and the projected size of the light coming from the projector. A light intensity test was performed in order to determine the power of the light that will cure the resin. Finally, a uniformity test was performed in order to determine if the light intensity across the entire projection area was consistent. All tests were performed with the CEL-5500 projector and the 5x reduction lens located at constant focal length.

#### 2.2.1.1 Optical resolution

The optical resolution of the system was measured by projecting a circle of a known diameter onto a Canon 60D DSLR camera. A picture was also taken of a microscope calibration slide in order to determine the actual size of the projected circle. The diameter of the circle image that was projected was 100 pixels. Measuring the calibration slide and the projected circle resulted a conversion ratio 7.60 μm/pixel when 5x reduction lens was used. This means that a single pixel on a digital image projected by the projector will

have a length of 7.6 µm and a width of 7.6 µm. Different conversion ratio can be obtained if a lens having different reduction ratio is used.

#### 2.2.1.2 Light intensity/ contrast

The light intensity of the projector was measured using a Coherent FieldMaxII light energy meter. A white circle with a diameter of 100 pixels on a black background was projected onto the light intensity measuring probe. The actual size of the projected circle was less than the sensor area of the probe. Using the raw power reading from the light intensity meter and the actual size of the projected circle, the light intensity can be measured.

The light intensity of a fully black image and of a 100 pixel diameter circle were both measured. The light intensity measured using the black image was 0.0016 $mW/cm^2$. The light intensity for the white circle was 15.69 $mW/cm^2$. The division of these two results gives a contrast between a white image and black image of 9806:1. A large contrast number (such as the result obtained here) is important for the correct curing of the resin. A low contrast of the system will result in unwanted areas of the resin curing during the printing process.

The light intensity through the PDMS slide was also measured, in order to determine the correct amount of light that the resin will receive during the actual printing procedure. In this case, the black image intensity was 0.001 $mW/cm^2$, the white image intensity was 14.79 $mW/cm^2$, and the contrast was 14787:1.

### 2.2.1.3 Uniformity

Determining the uniformity of the projection system is important in order to determine if any parts of the projection area have unusually high or low light intensities. In order to determine this, 9 different squares with lengths and widths of 100 pixels were projected, and their intensities were measured. The projected squares in their correct locations, and the measured light intensities at those locations are shown in FIGURE 2.11.

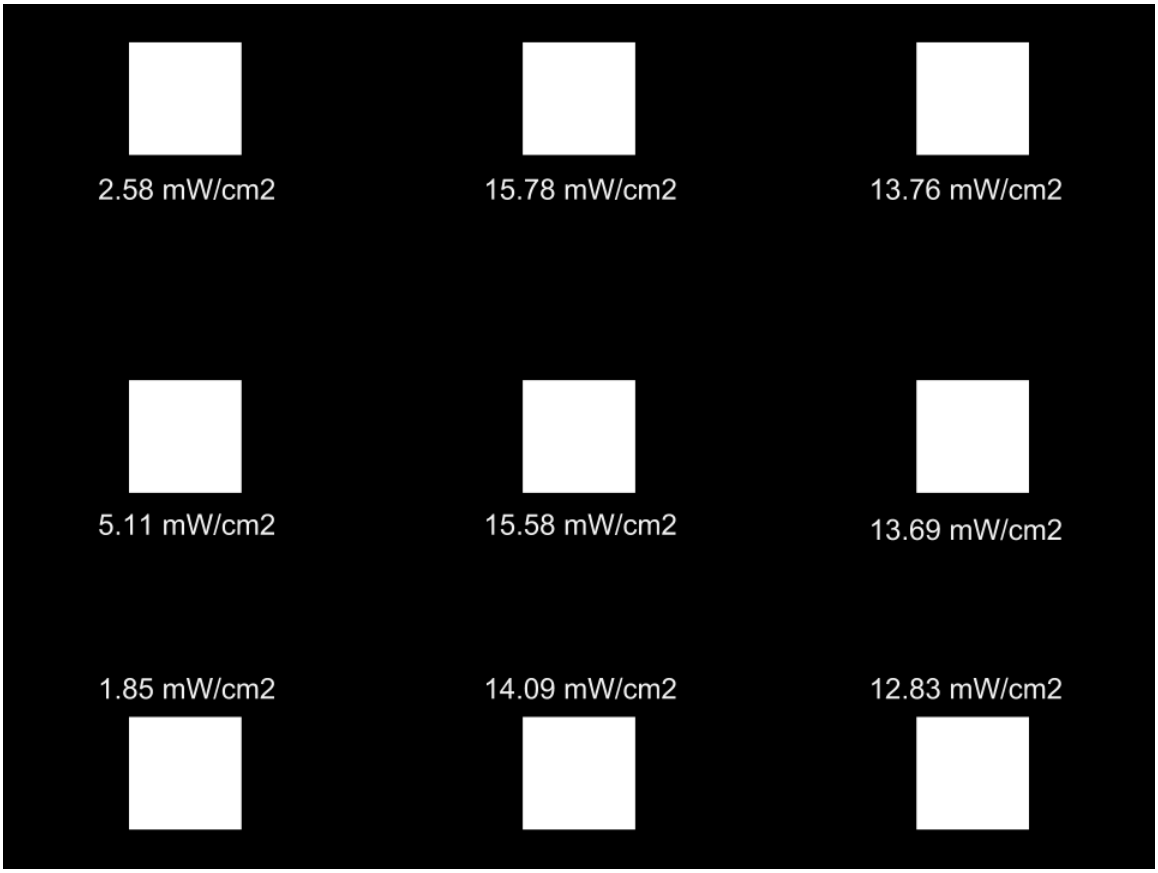


**FIGURE 2.11: Light intensity uniformity results on the projection focal plane**

As shown in FIGURE 2.11, the light intensities on the left side of the projection area are unusually low. In order to assure good light uniformity for the printed parts, the left side of the projection area will not be used. A width 200 pixels on the left side of the projection area will not be used. This poor uniformity of the system is most likely caused by an improper alignment of the 5x reduction lens with the internal optical path of the projector. The light intensity measurements in the center and the right side of the image area good, with only a 17.7% difference between the highest value (15.78 $mW/cm^2$) and the lowest value (12.83 $mW/cm^2$).

### 2.2.2 Material delivery

One of the most important parts of this system is the ability to extract precise and small volumes of resin. The smaller and more precise the resin droplet formation, the less material waste that the system will produce. For these reasons, an emphasis was placed on the design of the resin droplet system. The droplet system should be able to work with a wide variety of resins with varying viscosities. The system must also be scalable, so that the system can be sized up or down depending on the application. Repeatability of the system is also very important, as the droplets will need to be precisely extracted to a predetermined volume each and every time.

#### 2.2.2.1 Mechanical design of the system

The mechanical design of the resin delivery system is shown in FIGURE 2.12. Resin is held under pressure in 1/16” ID / ⅛” OD silicone tubing. In order to apply desired pressure to the resin, pressured air is used. An omega PRG200-25 pressure regulator is used to regulate and drop the incoming air pressure. The pressurized resin is allowed to flow when a pinch valve (075P2NC-12-02S, Bio-Chem Fluidics, Boonton, NJ) is opened.

The pinch valves simply pinch the silicone tubing to prevent fluid flow. When voltage is applied to the valves, the tubing is released and the resin can flow. The resin flows through a polypropylene dispensing needle tip that is attached to the silicone tubing by a luer lock to barb fitting. The dispensing needles can be bought in different opening sizes so that less or more material can flow through the tip. The nozzles for all of the testing done with the system were 25 gauge dispensing tips with a 0.012” diameter opening, and a length of 18.15mm. In order to lower and raise the nozzles to and from the platform, a nozzle movement stage was built. The linear bearings for this were made of PTFE impregnated delrin, the main construction was machined from polypropylene, and the whole stage rides up and down on ceramic coated aluminum rods. The whole assembly moves up and down with the rotation of the servo motor. During operation, the servo motor rotates 60 degrees to lift the droplet nozzles up by 5mm.

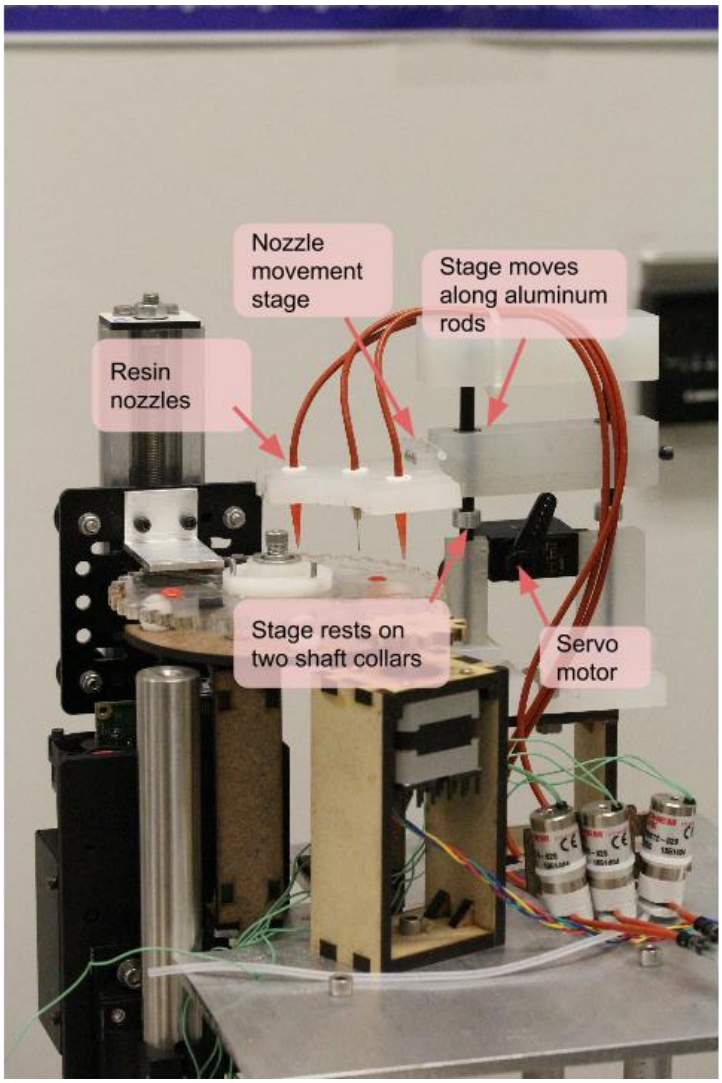


**FIGURE 2.12: Mechanical design of the resin droplet system**

### 2.2.2.2 Theory behind droplet deposition

In order to effectively control the amount of resin that will be deposited by the resin droplet system, the theory behind the flow of resin must be understood. In order to simplify the model of resin flow through the nozzles, some assumptions are made. The assumptions made are that there is laminar flow in the nozzle, fully developed flow, constant properties in the resin, and that the resin is incompressible. Based on these assumptions, the flow rate can be calculated as follows, where Q is the flow rate of the

resin, μ is the viscosity of the resin, L is the length of the nozzle, D is the inner diameter of the nozzle, and ∇p is applied pressure on the resin.

$$Q = \frac{\pi \Delta p D^4}{128 \mu L} \quad [1]$$

Since short valve opening times (from 25ms to 300ms) are used for the resin droplet calculations, the fully developed flow assumption may not be entirely accurate. This assumption will be tested in the experimental results section. The equation shows that the flow rate will be linearly dependent on the viscosity, pressure, and valve opening time. These parameters can be changed in the system and their effect on the flow rate of the resin will be studied.

#### 2.2.2.3 Experimental results

The viscosities of the three resins that were to be tested in the liquid droplet system were measured. This was done to ensure that accurate viscosity data for these materials was obtained to allow the results from the subsequent droplet testing to be compared to a theoretical model. The viscosities of PEGDA 250, HDDA, and PEGDA 575 were measured. The viscosities of the resins were recorded at room temperature (~80ºF). The instrument used was a Brookfield engineering viscometer. A sample of resin (~5mL) was placed in the machine, and then a metal cylinder was laid in the cylinder and attached to the load cell. The metal cylinder is rotated, and the resistive force is measured. Depending on the geometry of the setup, which is known, the viscosity can be calculated. Twenty readings are averaged for each data point that is recorded. The results of the viscosity testing is graphed in FIGURE 2.13. The viscosity of HDDA is 6.30 ± 0.60 cP,

PEGDA 250 is 13.4 ± 0.41 cP, and PEGDA 575 is 58.7 ± 1.17 cP. These viscosity measurements matched viscosity data given by the manufacturers.

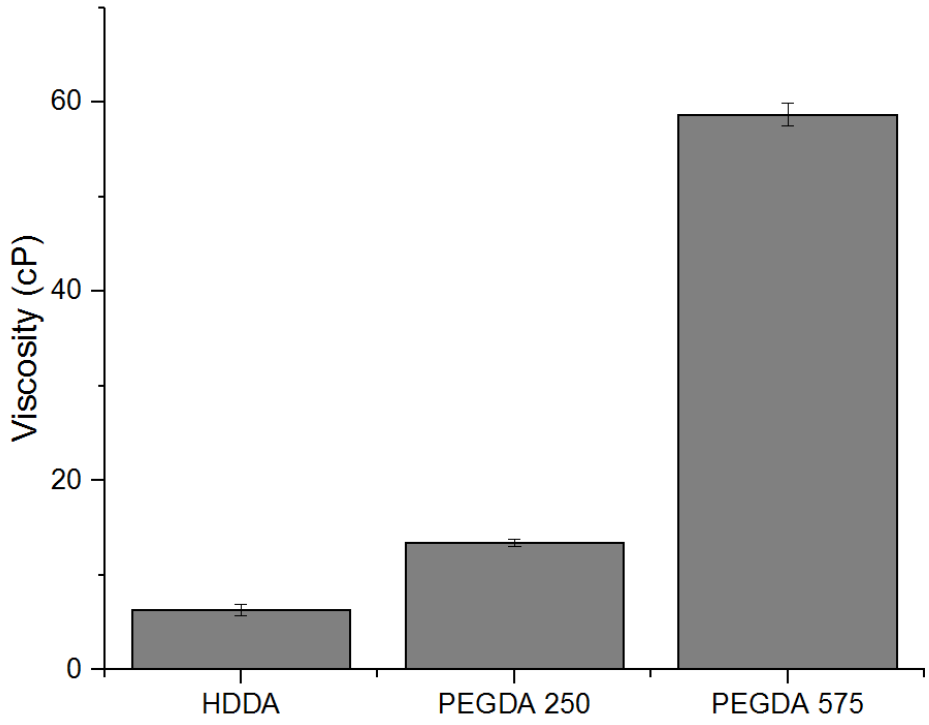


**FIGURE 2.13: Viscosity measurements for HDDA, PEGDA 250, and PEGDA 575**

The droplet size of the liquid resin must be precisely controlled in order to minimize material waste while ensuring that sufficient resin is delivered to the build area. In order to test this, resin droplet volumes were measured for all three resins at varying pressures and pinch valve opening times. For each combination of pressure and calve opening time, 8 droplets were formed. A Canon 60D DSLR camera held at a fixed point was used to image the droplets after they were formed. Image J was used to measure the area of the droplets. The volume of the droplets was calculated assuming a spherical cap shape. The results from the resin droplet tests are shown in FIGURES 2.14 and 2.15.

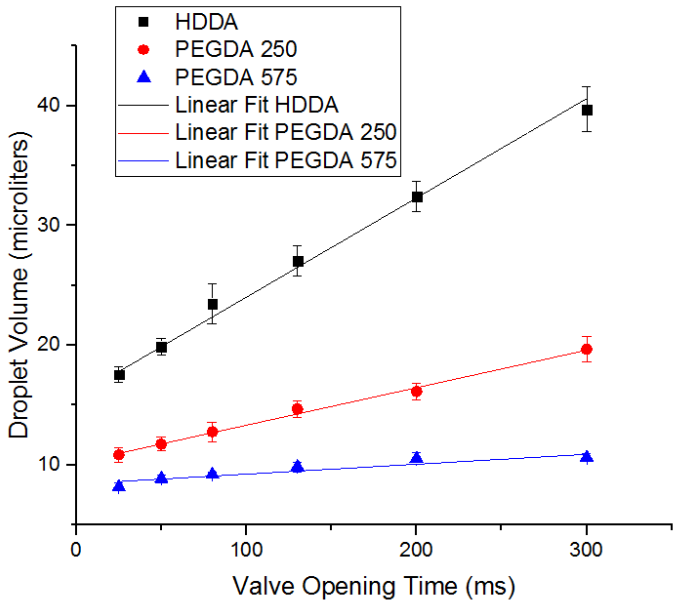


**FIGURE 2.14: Droplet volume vs. valve opening time at 2psi**

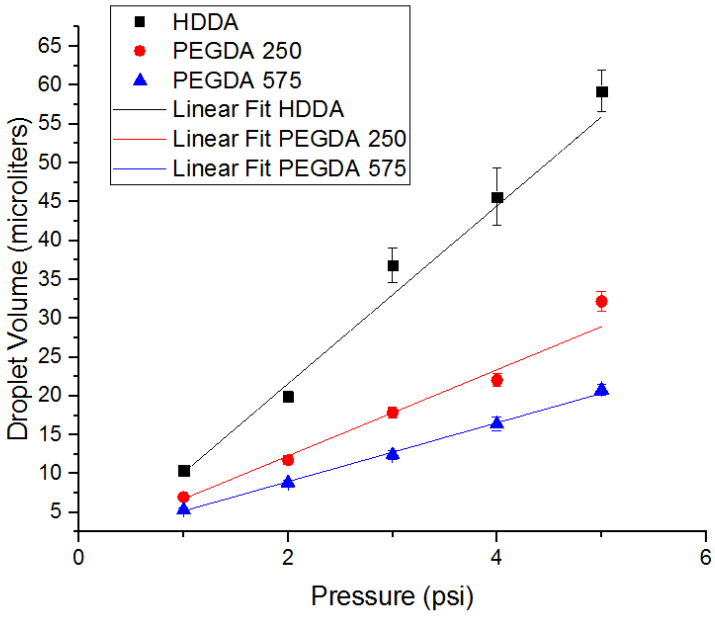


**FIGURE 2.15: Droplet volume vs. pressure at valve opening time of 50ms**

The results for the droplet delivery tests show a strong linear relationship between droplet volume and pressure and droplet volume and valve opening times, as was predicted by the flow rate equation for a viscous fully developed flow. These graphs can be used to predict the necessary parameters for a specific droplet size that is needed. The lower end of these graphs are more relevant for this printing system. For a full sized image (1024x 768 pixels) with a layer height of 100µm, the required material is 3.53 µL. A larger droplet volume, ~2x as much, should be used in order to ensure full coverage of the projected area. The flow rate equation also predicts that the flow rate will increase linearly with a linear increase in viscosity. To test this relationship, the volume vs valve opening time and volume vs pressure slopes were graphed versus viscosity. If there is linear relationship between flowrate and viscosity, then the graphs in FIGURE 2.16 will display a linear trend, which they do.

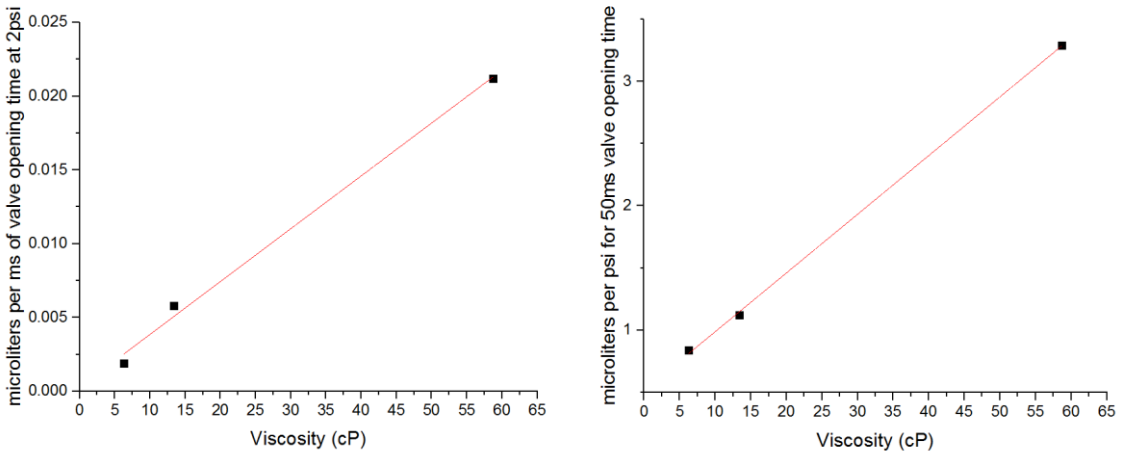


**FIGURE 2.16: Linear relationship between slope and viscosity**

### 2.2.3 Polymer curing

The performance of the system with regards to the curing of the polymer must be characterized. Even though the projection system can be used to project very fine features, the curing of the resin may not be as accurate due to polymerization kinetics, and so a resolution test is performed to characterize lateral printing resolution. It is also important to understand how long it takes to cure a certain depth of resin in the system to characterize vertical resolution of the printing system. Understanding how curing depth depends on photo absorber concentration and curing time will allow the correct curing time to be selected without going through trials and errors with under cured and over cured parts.

#### 2.2.3.1 Lateral resolution test

The goal of the resolution test is to determine the finest lateral feature that can be printed. To test this, suspended grids of decreasing pixel sizes are projected until the suspended grids no longer shoe empty space where no image is projected. FIGURE 2.17 shows how the resolution test is performed. The first layers printed are support layers that will hold the suspended grid. The final image printed is a fine grid. The width of the grid is set to a certain number of pixels. The grid sizes used in this experiment were 380 μm, 190 μm, 114 μm, 76 μm, and 38 μm. The curing time for each of these trials was 4.9 seconds per layer.

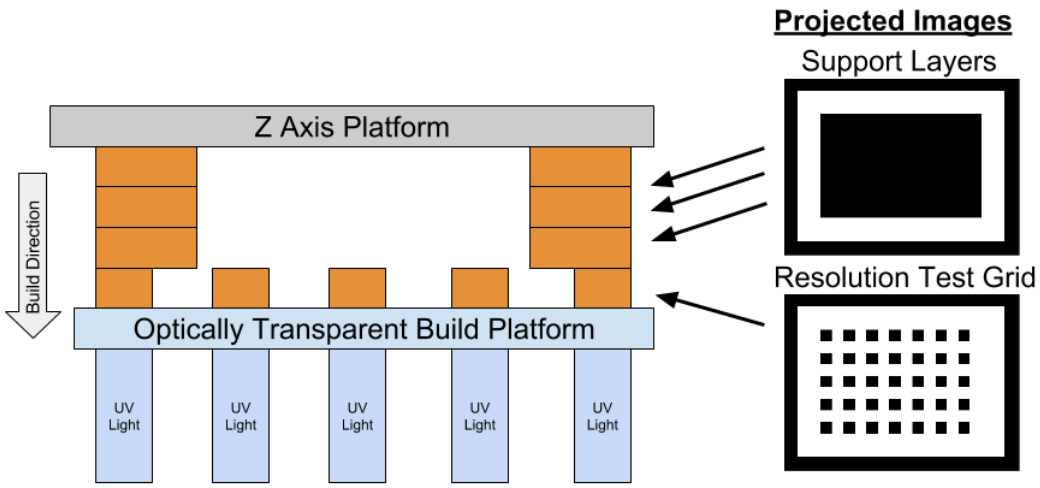


**FIGURE 2.17: Lateral resolution testing procedure**

Once the suspended grids are printed, they are then observed using a microscope. The results are shown in FIGURE 2.18. The 380 μm grid, 190 μm grid, 114 μm grid, and 76 μm grid are very clear, with the correct amount light shining directly through the portion of the grid where no image was projected. The grid for the 38 μm pixel grid is not as clear. In the 38 μm grid structure, the area of the grid that should have open space has some cured resin blocking the light. From these results we can see that the minimum feature size that can be printed perfectly is 76 μm.

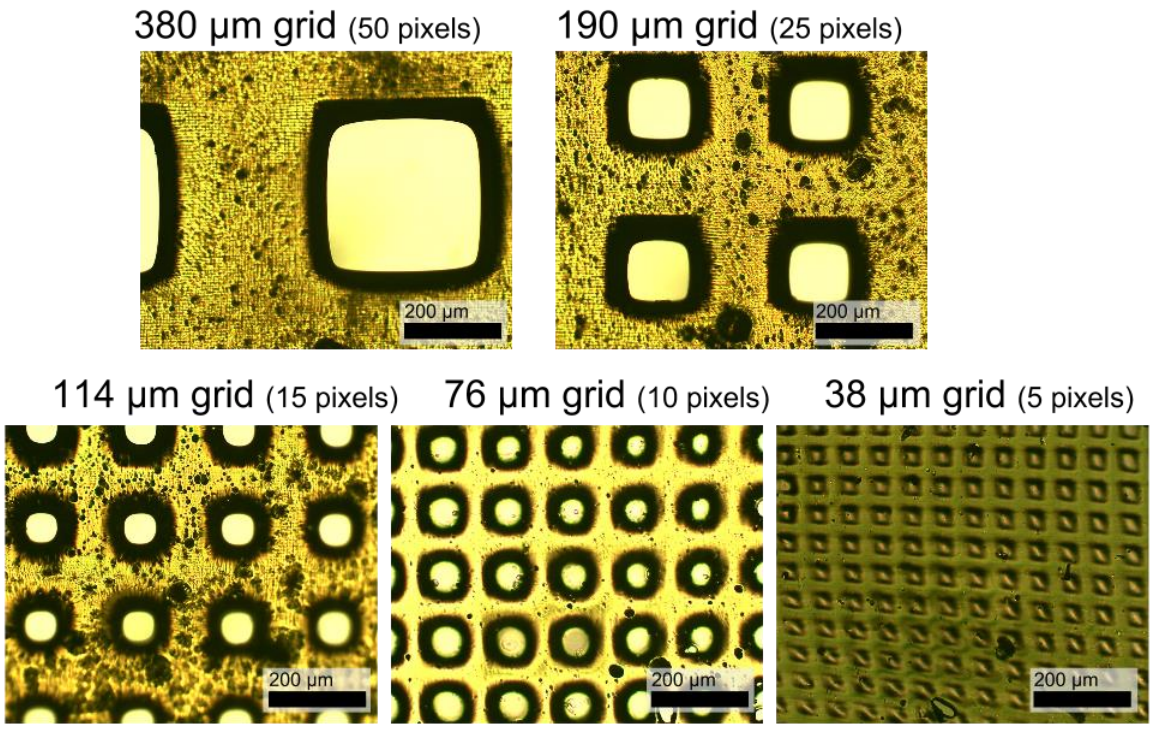


**FIGURE 2.18: Results of the lateral resolution test**

### 2.2.3.2 Curing depth study

The goal of the curing depth study is to determine what depth of resin will be cured for a certain exposure of light. The structure used to test this has four legs with suspended bridges between the legs, as shown in FIGURE 2.19. This part allows for three bridge thickness measurements to be taken for each curing time. The supports on the side are spaced so that the bridges will not come into contact with each other. First, base layers are printed, and then support layers are printed. Every 6 support layers, bridge layers are printed in between the supports. The bridge layers are produced from a single exposure of light. Each successive bridge is produced with an increased length of light exposure, so that each bridge will grow to a different depth. The bridges are separated by 6 layers of supports so that the bridges are free to grow vertically in thickness. Each printed part

contains 6 different bridges, each with a different width. The curing time for each bridge is controlled with the LabVIEW code. As the UV light shines, the bridge begins to grow. The longer the light shines for, the thicker the bridge. The thicknesses of the bridge are measured using a microscope. Using this data, the curing depth vs exposure dosage can be determined.

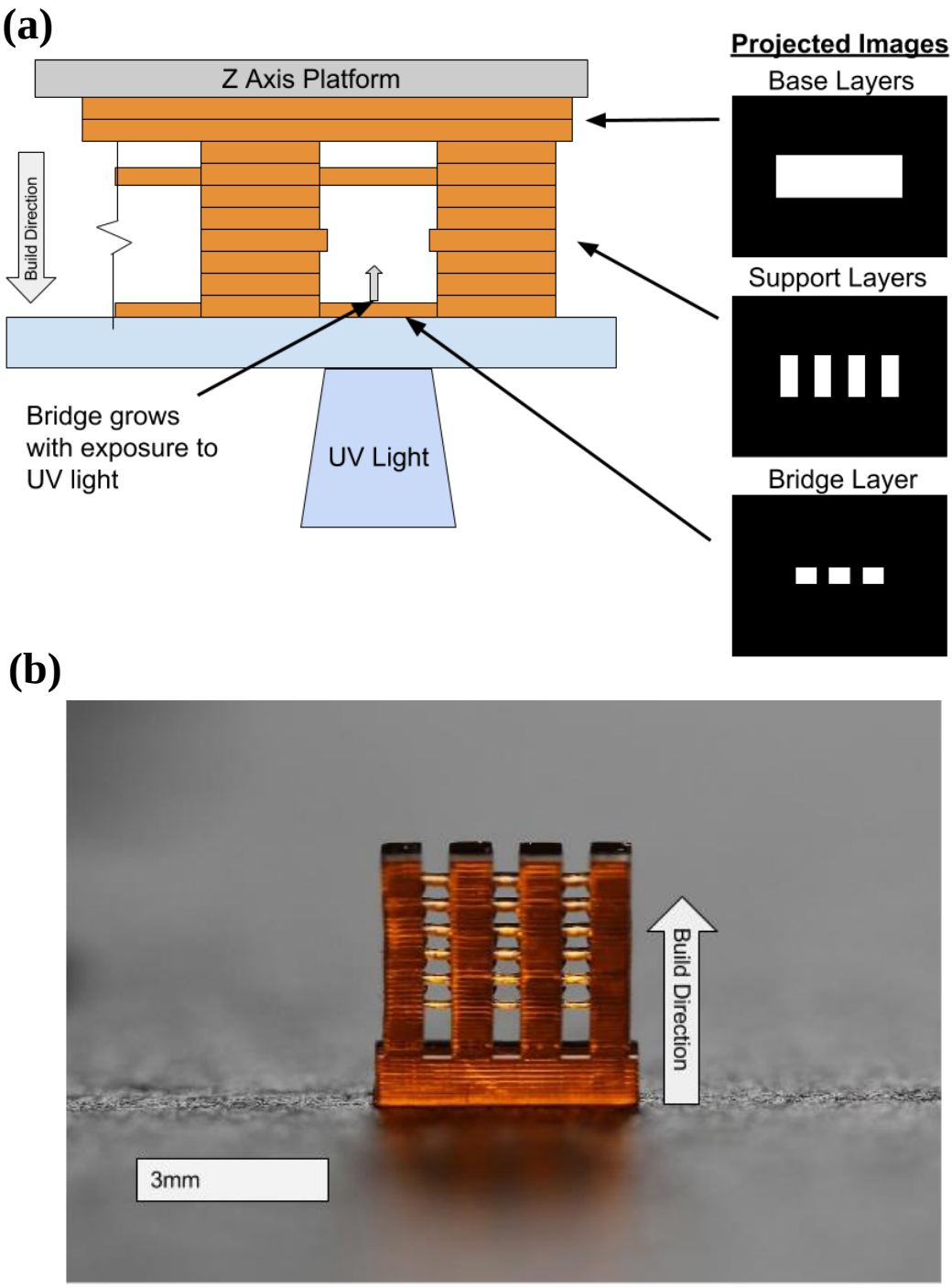


**FIGURE 2.19: Curing depth study (a) procedure for the printing of the curing depth bridge (b) picture of a curing depth study sample**

Curing depth studies were performed for three photo absorber levels (0.1%, 0.2%, and 0.3% of Sudan 1) in HDDA, PEGDA 250, and PEGDA 575 resin mixture containing 2% photo initiator. The curing depth for a photo initiated resin should follow the following curing depth relationship.

$$C_d = D_p \ln(\frac{E}{E_c}) \quad [2]$$

Here, $C_d$ is the cure depth of the resin, $D_p$ is the slope of the curing depth relationship, E is the applied light exposure, and $E_c$ is the amount of light exposure at which resin curing begins to occur. By graphing the curing depth of the resin as a logarithmic function of the exposure dosage, $D_p$ can be solved for. This key parameter will allow for the curing depth of the resin to be calculated given any light exposure or vice versa.

Graphing the exposure dosage on a logarithmic axis allows for a linear relationship between curing depth and exposure dosage to be found. Increasing the photo absorber levels reliable decreases the curing depth of the resin for a certain amount of exposure dosage. These plots (FIGURE 2.20, FIGURE 2.21, and FIGURE 2.22) can be used in order to reliably predict the correct curing times necessary to cure the PEGDA 250 solutions for and layer depth between 25μm and 200μm. One notable observation is that all of the resins take similar levels of light dosage in order to cure a certain layer thickness of resin. Also, as theorized, all of the curing depths for a certain level of PA follow a linear trend when graphed against light exposure dosage on a natural logarithmic scale.

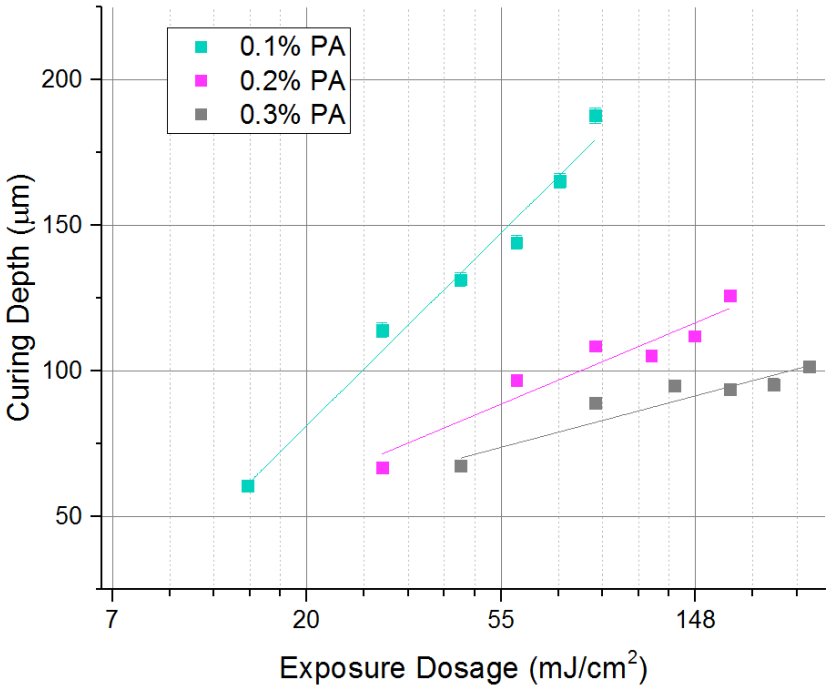


**FIGURE 2.20: Curing depth study result for HDDA**

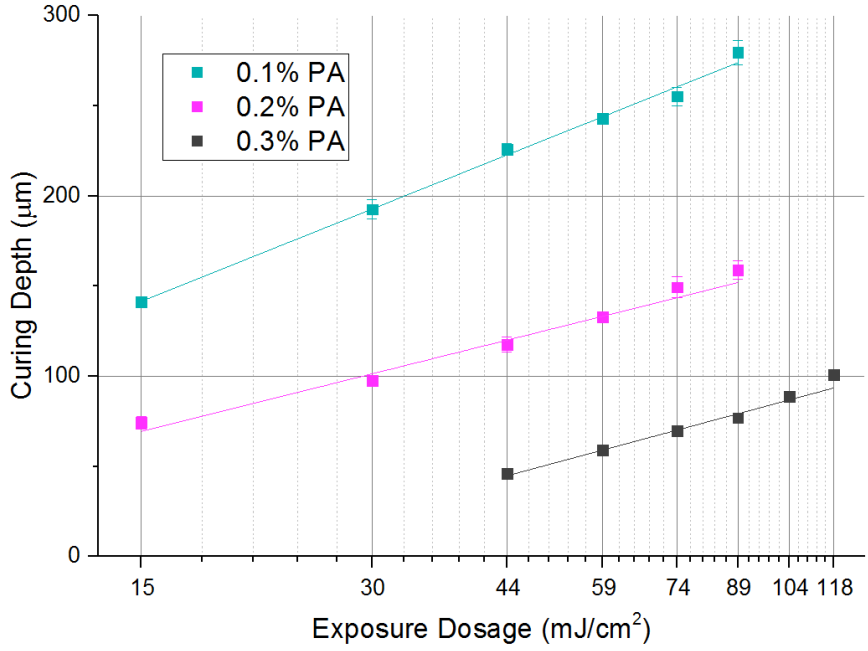


**FIGURE 2.21: Curing depth study result for PEGDA 250**

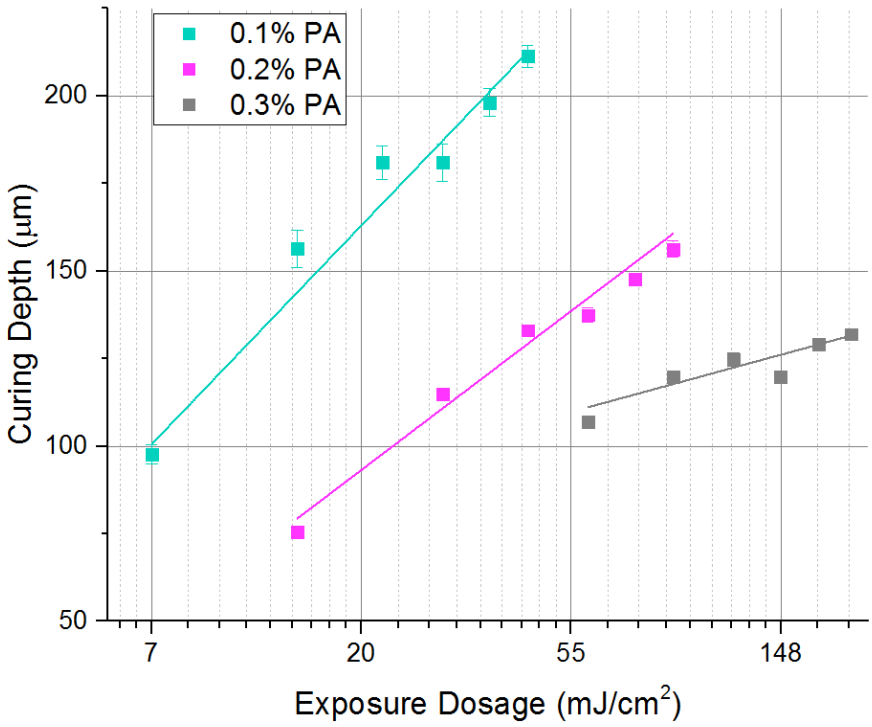


**FIGURE 2.22: Curing depth study result for PEGDA 575**

Graphing the curing depth curves against a natural logarithmic x axis allows for $D_p$ for $E_c$ to be solved for. $D_p$ is the slope of the curing depth curve and $E_c$ is the intercept that the curve makes with the x axis, which is the critical amount of light that it takes to begin curing the resin. The results for $D_p$ and $E_c$ for all three resins are shown in TABLE 2.2. The highest slope corresponds to the lowest concentration of photo absorber, and the lowest slope corresponds to the highest concentration of photo absorber. This relationship is consistent across all of the resins, except for PEGDA 250, where the slope remains nearly constant for the 0.3% and 0.2% PA concentrations. This relationship can be used to help predict curing times for resins with different levels of photo absorber. The critical light dosage lies between 0 and 18mJ/cm$^2$ for all of the resins and PA concentrations.

| Material | PA % | Slope ($D_p$) | $E_c$ (mJ/cm$^2$) |
|---|---|---|---|
| HDDA | 0.1% | 66.0 | 5.9 |
| HDDA | 0.2% | 27.9 | 2.3 |
| HDDA | 0.3% | 17.7 | 0.8 |
| PEGDA 250 | 0.1% | 73.9 | 2.2 |
| PEGDA 250 | 0.2% | 46.1 | 3.3 |
| PEGDA 250 | 0.3% | 49.6 | 18.0 |
| PEGDA 575 | 0.1% | 62.5 | 1.5 |
| PEGDA 575 | 0.2% | 45.4 | 2.6 |
| PEGDA 575 | 0.3% | 16.3 | 0.1 |

**TABLE 2.2: Curing depth study parameter results**

These results can be used to predict curing times necessary to cure any structure using HDDA, PEGDA 250, or PEGDA 575. The linear trends can be used to approximate a necessary curing time for a certain layer thickness, or a certain PA level. These results are important not only for a characterization of the resins used, but also help eliminate guessing when deciding the necessary process parameters to build a certain structure.

### 2.2.4 Multiple material bleed over

In order for a multiple material 3D printing to be effective, the separation between the different printed materials must be distinct. In order to show the material bleed over between two materials during the printing process, a multiple material bleed over test was devised.

#### 2.2.4.1 Multiple material bleed over test

The multiple material bleed over test will show how one material bleeds into another when printing with multiple materials. The effect of the cleaning droplet on the amount of material that bleeds over will be determined.

The bleed over test is performed by projecting two interlocking checkerboard images, one for a PEGDA 250 solution with 0.1% rhodamine b, and one for a PEGDA 250 solution with 0.1% $DiOC_2$. The images and desired outcome of the experiment are shown in FIGURE 2.23.

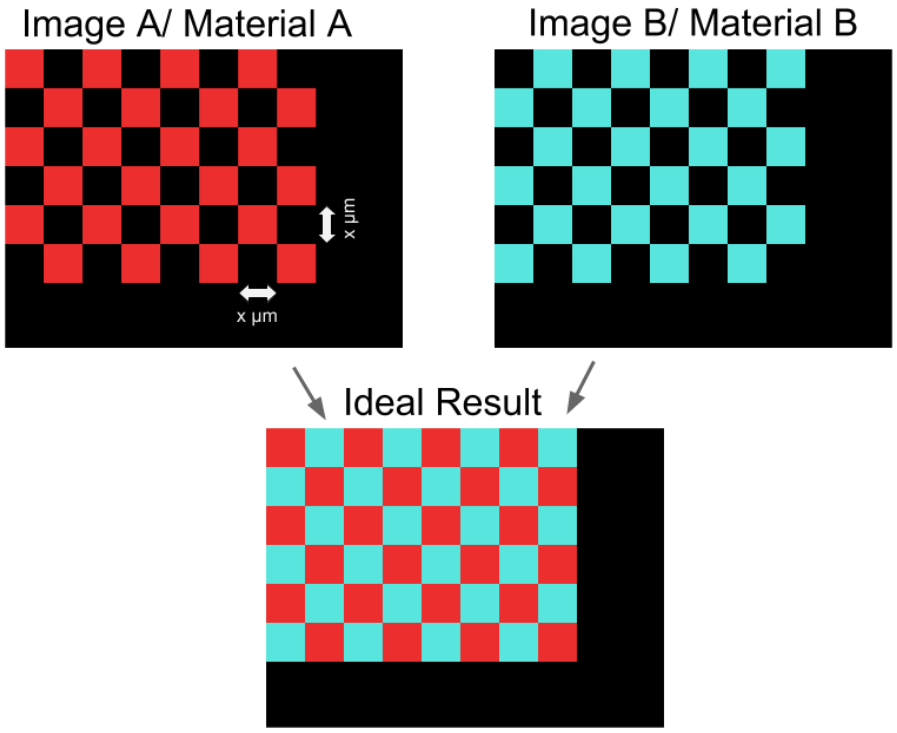


**FIGURE 2.23: Multiple material bleed over experiment**

Both images are printed in a single layer on top of a glass slide. For the tests without the cleaning droplet, the first image is printed and then the second image is printed immediately after. For tests with the cleaning droplet, after the first image is projected, the layer is dipped in a droplet of ethanol before the stage is lowered onto the second material and the second image is projected. Fluorescent microscopy was used to show the bleed over of the resins for projected grids of 1520, 760, 380 and 190 μm widths for processes with and without cleaning droplets. When excited with the correct wavelength of UV light, $DiOC_2$ fluoresces blue and rhodamine b fluoresces pink. The fluorescent microscope used is a monochrome fluorescent microscope, so each fluorescence is captured separately, colored with the correct color, and then layered over the original image.

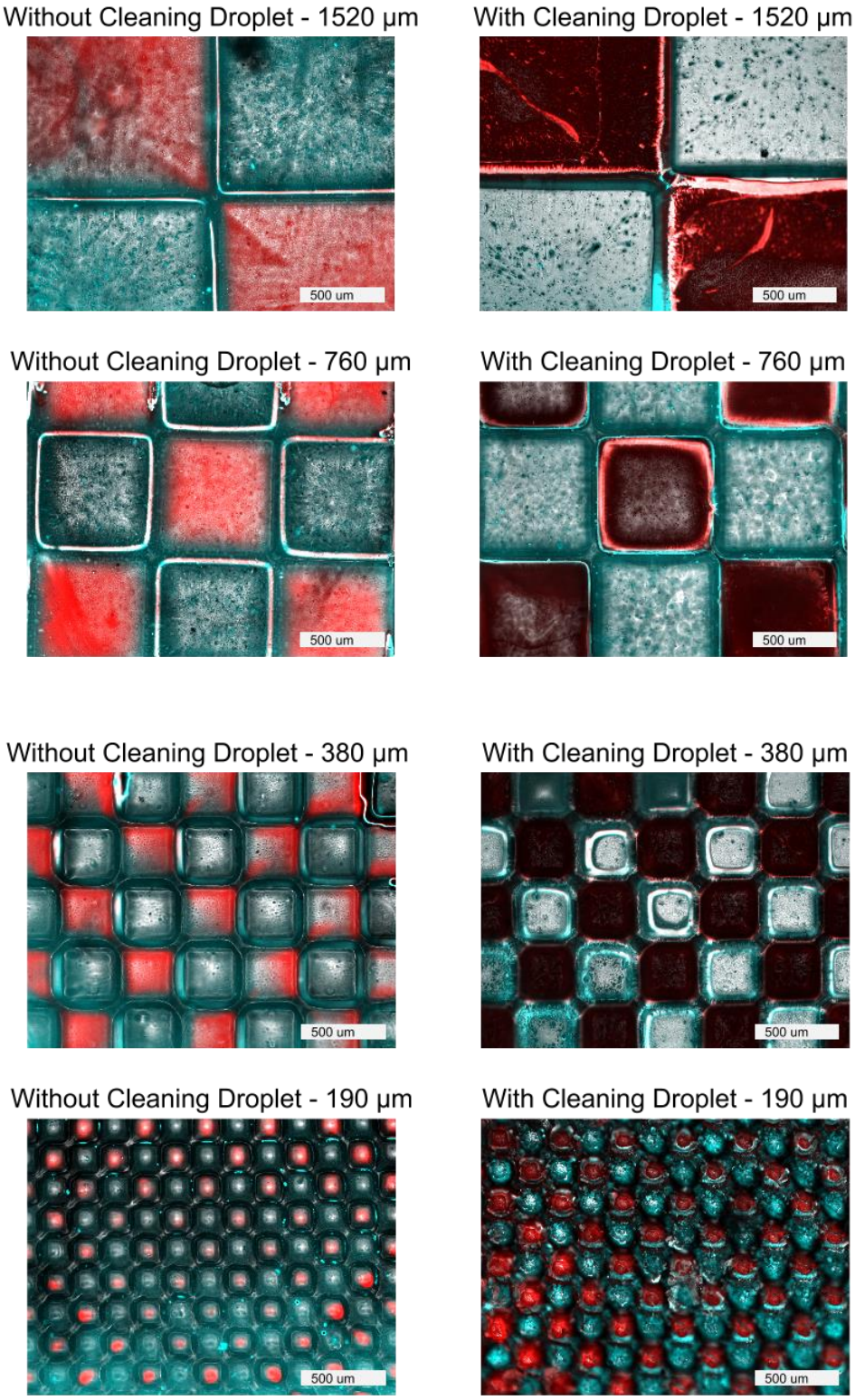


**FIGURE 2.24: Multiple material bleed over testing results**

The results of the multiple material bleed over testing are shown in FIGURE 2.24. Since the resin containing $DiOC_2$ was printed first, leftover $DiOC_2$ will bleed over into the rhodamine b squares. This bleed over is very clearly apparent in the cases without a cleaning droplet.

Measurements of the material bleed over were taken using image analysis in order to quantify the proportion of material bleeding over into the other. For good multiple material performance, we have determined that a bleed over fraction greater than 0.5 is unacceptable. In order to measure the fraction of bleed over in each trial, first square boundaries were drawn where the rhodamine b containing resin should be. The area of bleed over of $DiOC_2$ dye in the boundary was divided by the total area of the square to calculate the bleed over fraction. To determine the boundary where the $DiOC_2$ dye ends and the rhodamine b dye begins, a line is drawn in the middle of the grey area between the two brightly defined dyes. An example of this measurement for the 760 μm grid without the use of cleaning droplets is shown in FIGURE 2.25. At least 1/8 of the total image was used to calculate the bleed over results, which are tabulated in TABLE 2.3.

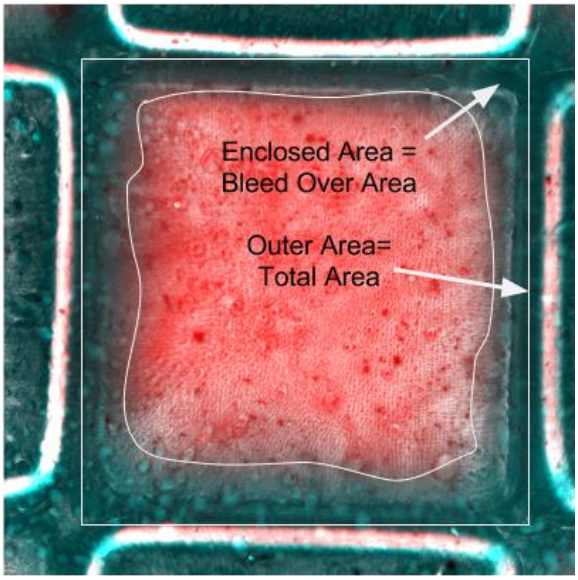


**FIGURE 2.25: Measurement to determine the bleed over fraction**

| | Bleedover Fraction | |
|---|---|---|
| **Grid Size** | **Without Cleaning Droplets** | **With Cleaning Droplets** |
| **1520 µm** | 0.215 | 0.058 |
| **760 µm** | 0.347 | 0.100 |
| **380 µm** | 0.504 | 0.152 |
| **190 µm** | 0.813 | 0.496 |
| | | |
| | = unacceptable bleedover (>0.50) | |

**TABLE 2.3: Multiple material bleed over results**

The results of the bleed over test show a strong decrease of material bleed over when a cleaning droplet is used. Without a cleaning droplet, feature sizes smaller than 380 µm cannot be correctly reproduced. With a cleaning droplet, feature sizes can be correctly reproduced all the way down to a feature size of 190 µm. As determined earlier, the minimum resolution that can be cured is 114 µm. The cleaning droplet may fail to provide good results for this fine of a structure, so improvement to this result should be

attained in the future. One way to improve the performance of the cleaning droplet system is to increase the size of the cleaning droplet in order to allow for better diffusion of the remaining resin.

## 2.3 3D Printing results

The most important part of characterizing a 3D printing system is the actual printing of objects. First, single material objects were printed using solutions of HDDA, PEGDA 250, and PEGDA 575 resins. Then, multiple material prints were made and the material usage was for those prints were compared to competing multiple material systems.

### 2.3.1 Single material prints

The single material prints of micro lattice structures were made using solutions of HDDA, PEGDA 250, and PEGDA 575. Each resin solution used 2% photo initiator, and 0.2% photo absorber (Sudan 1 dye). FIGURE 2.26 shows the final printed parts from the system. All 3 parts have a layer thickness of approximately 100μm and use a curing time of 4.9 seconds per layer. The final printed parts correctly show the desired micro lattice structure.

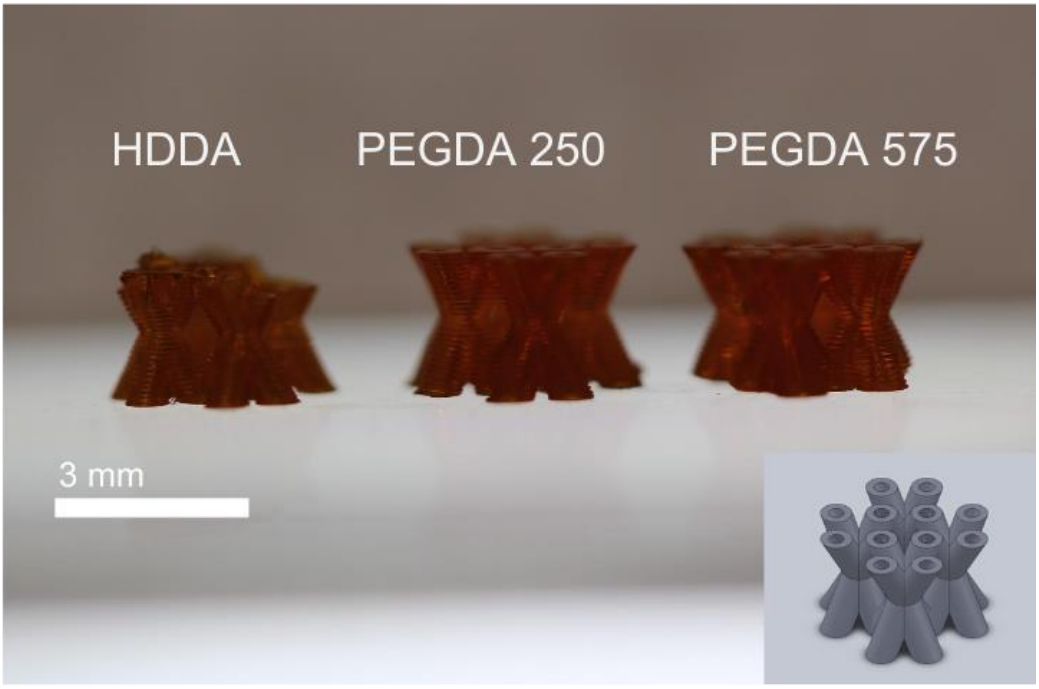


**FIGURE 2.26: Single material 2x1 unit cell structures**

More single material prints were made using HDDA, PEGDA 250, and PEGDA 575 resins with 0.2% PI and 0.1% PA. The layer thicknesses for the following structures were all 58.3 μm, which required a curing time of 2.9 seconds. FIGURE 2.27 shows a replica of the Whitehouse made with HDDA resin. There are 20 layers in this structure. The next resin, PEGDA 250, was used to make a replica of the Eiffel Tower as shown in FIGURE 2.28. There are 174 layers in this structure. PEGDA 575 was used to make a replica of a Mayan Temple. This structure is shown in FIGURE 2.29 and contains 34 layers. All of these replicas are highly accurate and show the very fine resolution possible with the printing system.

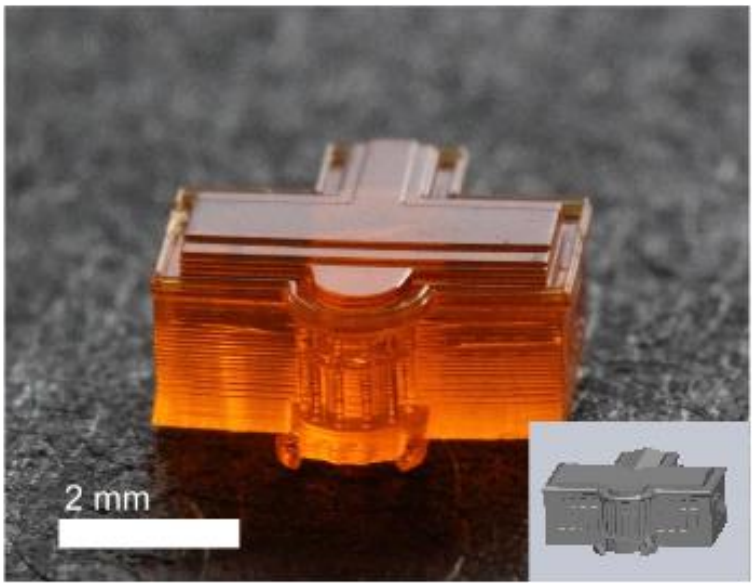


**FIGURE 2.27: Replica of the Whitehouse made with HDDA**

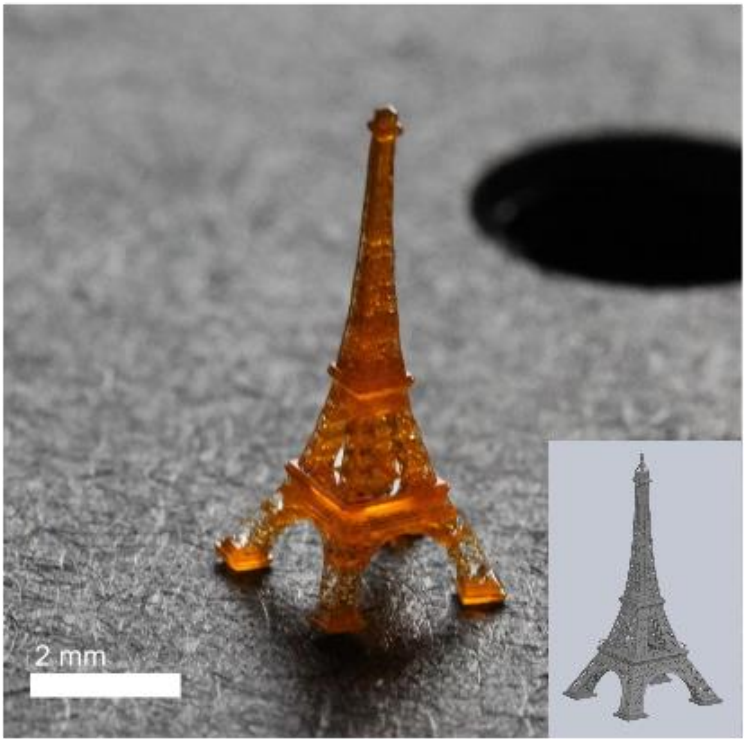


**FIGURE 2.28: Replica of the Eiffel Tower made with PEGDA 250**

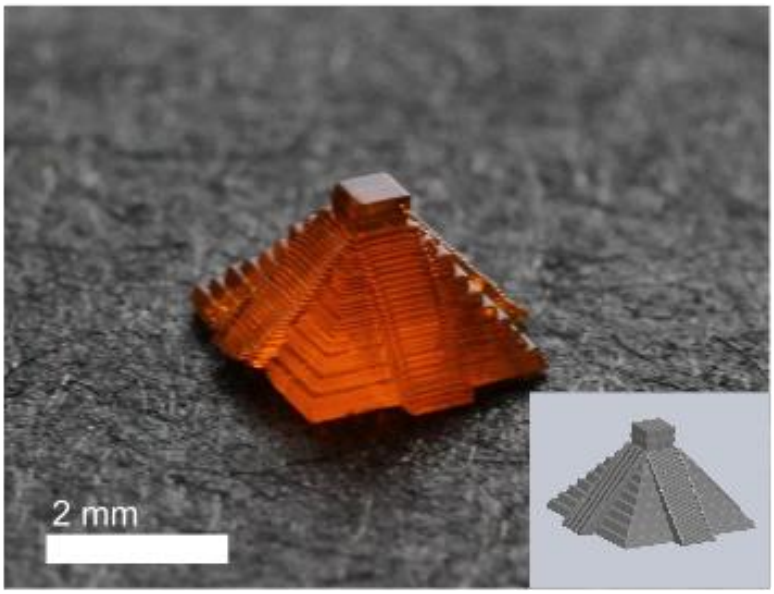


**FIGURE 2.29: Replica of a Mayan Temple made with PEGDA 575**

### 2.3.2 Difficult to print materials

One of the advantages of the droplet based multiple material 3D printer is the ability to work with difficult to print materials. One such material is a resin with a suspension of nickel flake. Nickel flake typically is difficult to print because it tends to come out of suspension and is extremely difficult to clean out of the printing system. The droplet based printing system is very easy to clean and allows for the resin to be mixed and deposited in a very short time frame, before the nickel flake comes out of suspension.

A part was made with a 1% by weight suspension of nickel flake in PEGDA 250 resin with 2% PA and 0.2% PI (Sudan I) to demonstrate the ability of the system to print this difficult solution. The result is shown in FIGURE 2.30. There are a total of 20 layers, each 58.3 μm thick. The curing time has to be almost doubled to 8 seconds per layer to cure the solution because the nickel flake blocks the UV light from the projector. The sample was tested with a magnet and found to be magnetic.

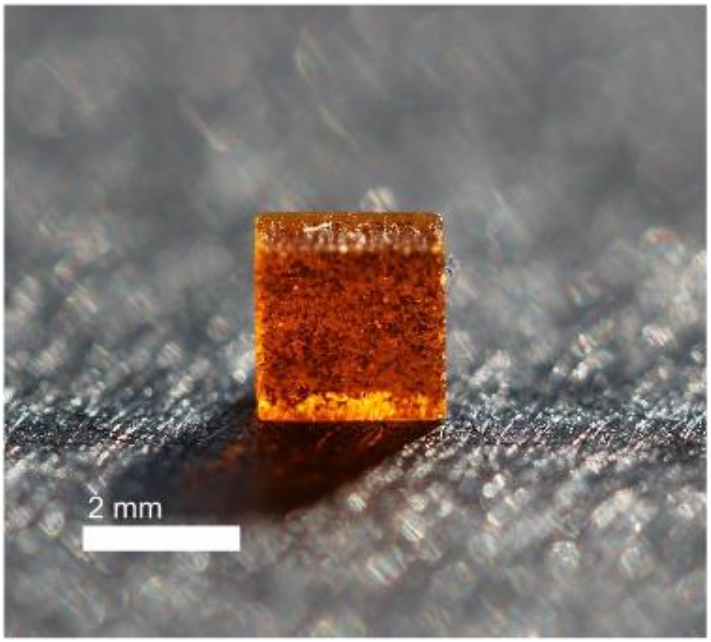


**FIGURE 2.30: Cured PEGDA resin with 1% by weight nickel flake suspension**

This nickel flake suspension can be used to make functional micro scale objects. By using a magnetic field, the parts can be manipulated in a specific fashion. One example of this is using a nickel flake loaded propeller to create fluid flow then the propeller is turned. As shown in FIGURE 2.31, a propeller was created from PEGDA 250 solution with 1” by weight nickel flake. There are 21 layers in the part. Each with a layer thickness of 48.3 μm. The propeller was spun from 0 to ~300 rpm on a magnetic stirrer in a bath of water. By adjusting the speed of the magnetic stirrer, flow in the water could be observed and adjusted. Other mechanical systems such as gears of actuators can be created using this same technique.

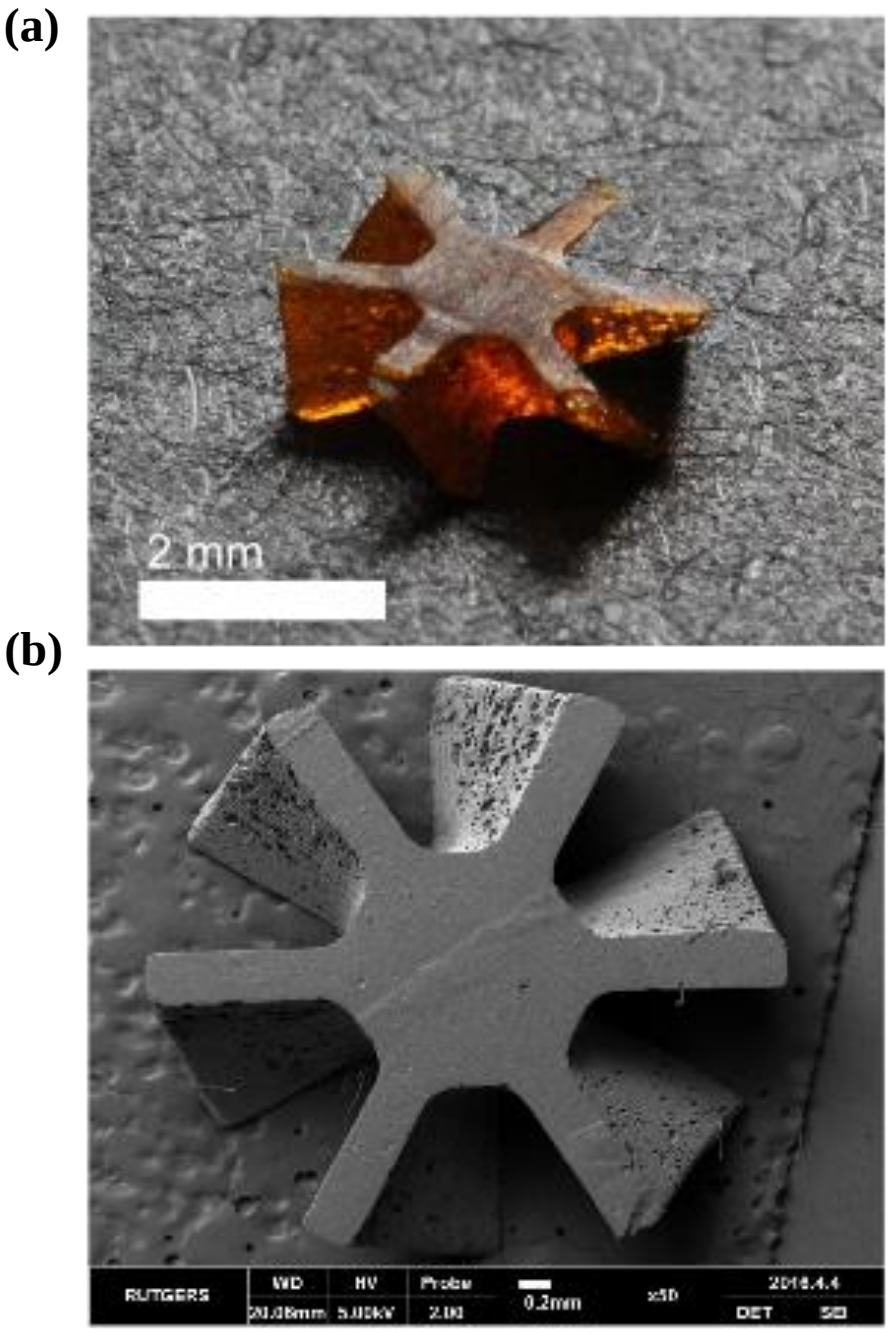


**FIGURE 2.31: Micro turbine made of PEGDA 250 with 1% nickel flake suspension (a) photo image of the turbine (b) SEM image of the turbine**

Another practical application where the droplet based multiple material 3D printing is advantageous is working with ceramic loaded reins. Like nickel flake, ceramic loaded resin is difficult to clean and can settle out of solution. The resin used for these tests was a PEGDA 250 based solution with a 5% suspension of $Al_2O_3$ powder, with a 15μm particle size, 2% PI, and 2% surfactant (sodium silicate, Sigma-Aldrich, St. Louis, MO). The fine alumina powder was purchased from Baikowski, Charlotte, NC. To demonstrate the use of ceramic loaded resin, a unit cell was printed. The unit cell has a 3x3x2 arrangement and was printed with a 1.5 second curing time per layer with a total of 81 layers, each with a thickness of 48.3 μm. The final printed part is shown in FIGURE 2.32.

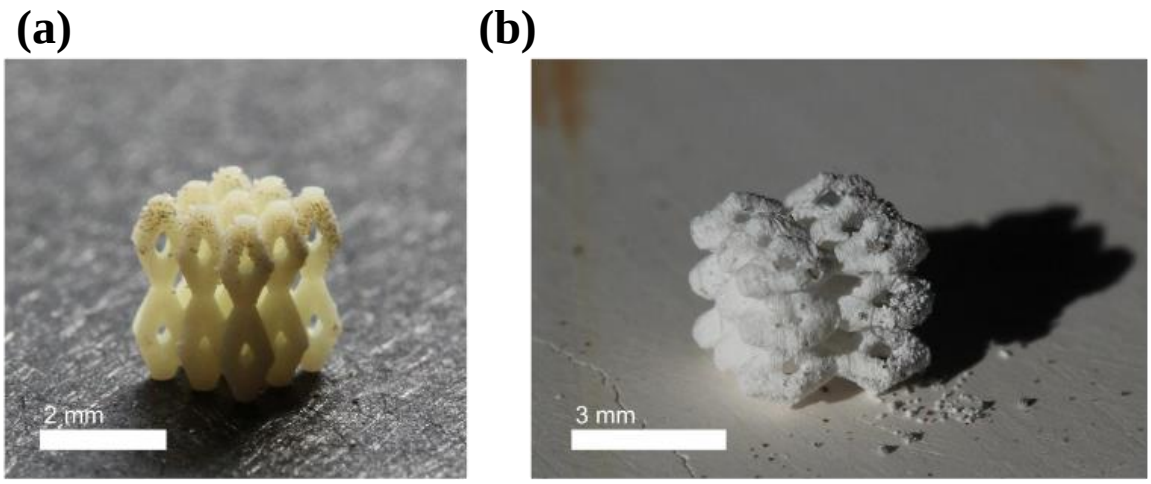


**FIGURE 2.32: Micro lattice made with alumina particle suspension (a) micro lattice before removal of polymer (b) micro lattice after the removal of the polymer**

The right side of FIGURE 2.32 shows the lattice after heating to remove the polymer, leaving the $Al_2O_3$ behind. The heating procedure is as follows; heat to 280ºC, hold 20 mins, heat to 250ºC, hold 15 mins, heat to 40ºC, hold for 20 mins, and finally heat to 630ºC at a rate of 18ºC/min and hold for 5 minutes. After this heating procedure, all of the PEGDA is visibly removed from the structure, leaving behind structure purely composed of $Al_2O_3$.

### 2.3.3 Multi material print and material usage efficiency

After correctly printing single material parts, the system was used to print multiple material parts. The two resins used for these multiple material parts both use PEGDA 250 with 2% photo initiator and 0.1% photo absorber. The photo absorber for the red material is rhodamine b and the photo absorber for the yellow material is $DiOC_2$. The object is a spiral with two arms that wrap around each other, each composed of a different material. The final printed part is shown in FIGURE 2.33. There are 34 layers in the part, and the curing time for each layer is 3.0 seconds. The arms of the spiral are clearly defined, and are very clearly composed of different materials.

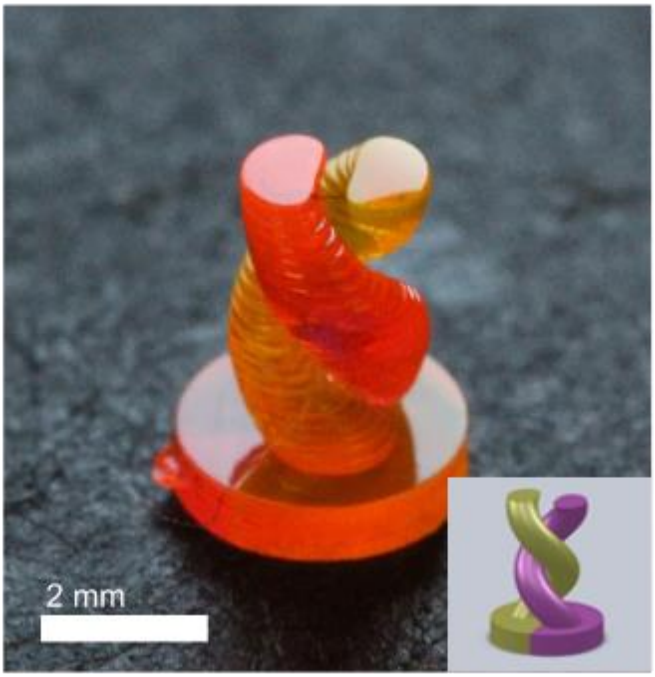


**FIGURE 2.33: Multiple material spiral print**

One advantage of incorporating multiple materials into a single object is the ability to use materials with different properties to create a final object with unique behaviors. The structure created and shown in FIGURE 2.34 has a micro architecture, that when paired with the correct materials, will experience a bulk negative expansion coefficient when heated. This type of behavior would not be possible in a single material part [23]. The structure is composed of 45 layers, and each layer was cured for 3.0 seconds.


**FIGURE 2.34: Multiple material object with tunable thermal expansion [23]**

The next multiple material printed part was used to show the material efficiency of the system when printing with multiple materials. The material efficiency of the system is defined as the volume of the printed part as a fraction of the total material used to create that part. The material efficiency of different systems can be compared to show the difference in material waste. The higher the material efficiency of the system the better. In order to test the material efficiency of the system, a Rubik's cube structure was printed as shown in FIGURE 2.35. The final printed part, has 20 layers, and each layer was cured for 3.0 seconds. Again, there is a clear distinction between the different materials in the part.

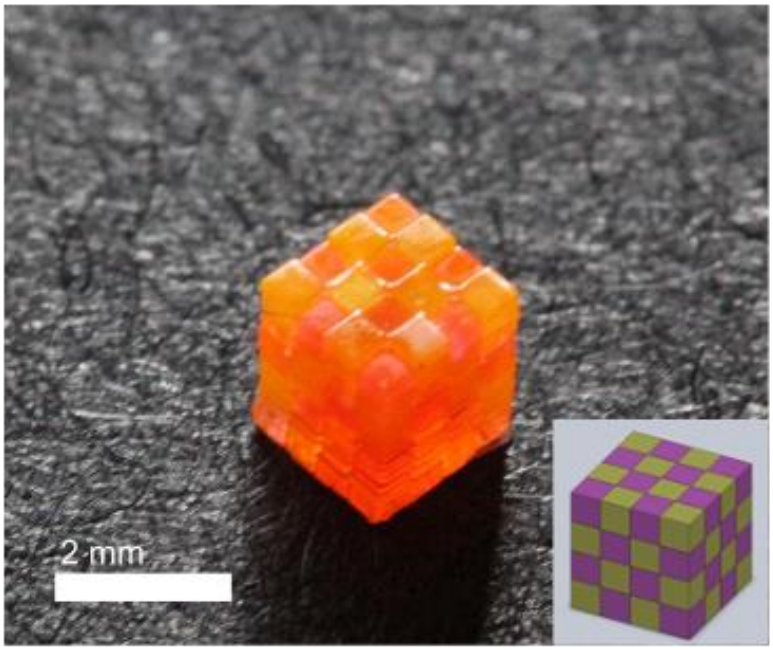


**FIGURE 2.35: Multiple material cube print**

FIGURE 2.36 shows the printed cube next to the amount of resin that was needed during the printing process. The resin used was approximately 0.07 mL, or approximately 8.75 times the volume of the printed part. The final volume of the printed part is 8.0 μL, making the material efficiency of the printer ~11.4% for this print. The amount of ethanol used as cleaning droplets was ~0.3 ml for this part. The part on the left hand side of FIGURE 2.36 was made with a chamber type multiple material system.

The chamber type system did not flush out the chamber with a pump after every layer, instead, the piston action of the sample stage was used to move resin in and out of chamber allowing the system to achieve its maximum material efficiency. In order to print a 2mm x 2mm x 2mm cube, 35mL of resin was used. This equates to a material efficiency of 0.023%, making the droplet based printing system 500 times more efficient in material waste than the competing chamber type system.

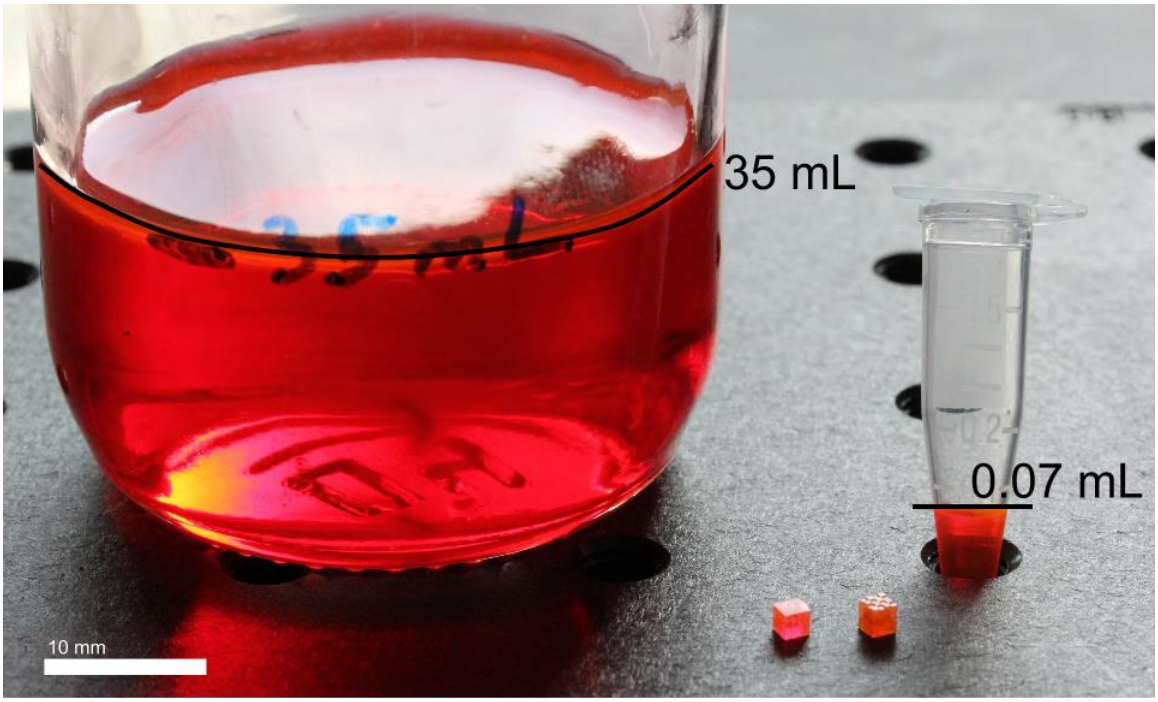


**FIGURE 2.36: Multiple material cube print compared to material usage**

## 2.4 Conclusion and comparisons

The ultimate goal of this research is to devise a multiple material 3D printing that exceeds the printing characteristics of competing systems. High resolution prints with features down to 76 μm in size have been demonstrated, proving that this system is gentile and accurate enough to print fine resolution parts, which resin vat systems and FDM printers have trouble with. Multiple material performance of the system has also been proven. Cleaning droplets have been shown to be an adequate method of reducing material bleed over so that multiple material parts can be accurately reproduced. The droplet based system has also been able to outperform competing systems in terms of material usage. The only other printing system capable of printing the same resolution of structures is the chamber system, which wastes large amounts of resin. The droplet based printing system has been demonstrated to waste 680 times less material than the material chamber system. In summary, characterization of the droplet based multiple material 3D printing system has led to the conclusion that this system significantly improves on the performance of competing systems by producing fine structures out of a variety of materials with minimal material waste.

# 3 Liquid Bridge Separation

Understanding and controlling material bleed over is a very large part of creating an effective multiple material 3D printing system. Material bleed over in this droplet based system is caused by leftover resin sticking to the printed part during the printing process. The cleaning droplet's job is to reduce this bleed over by diluting the remaining resin, but some of the cleaning droplet and the resin will still remain on the printed part after the object is drawn out of the cleaning droplet.

The separation of the remaining resin and cleaning droplet during the printing process is essentially a liquid bridge problem. The liquid bridge forms when the printed object lowers with the Z axis stage and comes in contact with the resin droplet. After the layer is printed, the stage recedes, and the liquid bridge is stretched until it breaks. In order to understand what portion of the droplet stays on the platform and what portion of the droplet stays with the printed part, liquid bridge separation must be studied.

## 3.1 Background

The model with which we study liquid bridge separation must closely match what is observed in the real liquid bridge breaking process. Contact angle hysteresis (a difference in the advancing and receding contact angles of the liquid bridge) was observed during the liquid bridge formation and separation processes. Previous studies developed a model for liquid bridge separation while taking contact angle hysteresis into account and found the numerical model results to closely follow the experimentally observed liquid bridge behavior [18]. FIGURE 3.1 shows the geometry of the liquid bridge, with the contact

radius $R_1$ on the top surface, the contact radius $R_2$ on the bottom surface, $\Theta_1$ on the top surface, and $\Theta_2$ on the bottom surface.

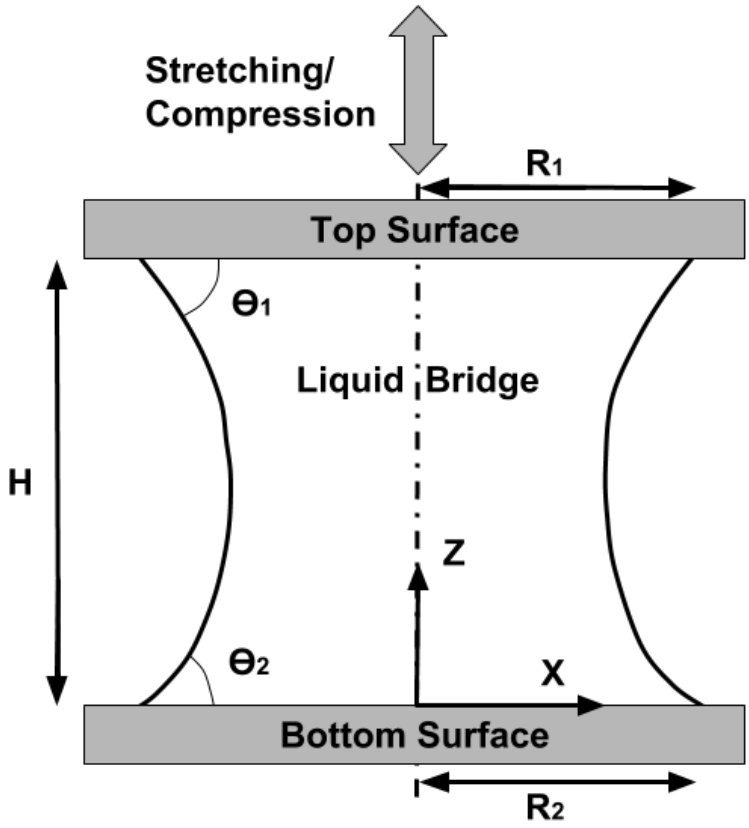


**FIGURE 3.1: Geometry and coordinate system of a liquid bridge in equilibrium between two solid surfaces**

As the liquid bridge separates, R1, R2, $\Theta_1$, and $\Theta_2$ adjust with the movement of the bridge. At the beginning of liquid bridge separation, the contact angle (on either surface) will increase as the bridge separates. The contact angle will continue to decrease until the receding contact angle is achieved, and at that time the contact angle will remain constant as the contact radius begins to decrease. According to this model, once the receding contact angle is reached, the contact line will continue to slip, and R will decrease until

the liquid bridge separates. The contact radius on the top and bottom surfaces do not necessarily begin to slip at the same times, the contact line only slips once the contact angle reaches the receding contact angle on that surface [18]. This model will be used to describe and understand the liquid bridge separation process that is observed in the droplet based printing system.

## 3.2 Motivation

Material bleed over is a significant problem in all current multi-material liquid resin based 3D printers. As demonstrated earlier, an ethanol cleaning droplet has been used to effectively reduce material bleed over, however this method is not without its drawbacks. The major drawback is that a foreign material must be introduced to the part in order to dilute the resin. In this case ethanol does not have a significant detrimental effect to the final printed part, however it could in other cases, especially those cases where expensive bio materials are used, and it may not be desirable to have ethanol in contact with the printed part.

Even with the usage of ethanol, some material and ethanol will remain on the part that is being printed. In order to reduce this leftover material, the liquid should fully remain on the printing surface as the part is drawn away. The requirement that the remaining material should adhere to the printing surface is contrary to the main purpose of the printing surface, which is that the printing surface should be nonstick in order to allow the printed material to be gently lifted away from the build platform.

These two contradictory requirements mean that the surface upon which the droplets sit should be nonstick during the resin curing surface, but attract the remaining resin while

the part is drawn away. A potential method of creating this reversible wetting is with electro-wetting. By applying a charge to the liquid droplet, and supplying a ground connection underneath a dielectric that the droplet sits on, the liquid droplet can be made to wet the surface when a high voltage is applied. The reversible nature of the electro-wetting system should allow the printing surface to remain nonstick while no voltage is applied, but will cause the excess resin to stay on the platform when voltage is applied and the Z axis recedes.

## 3.3 Liquid bridge study

A study of liquid bridge separation in the droplet based printing system was done in order to determine what the transfer ratio between different combinations of surfaces in the printing system would be. Studying this liquid bridge separation allows for better understanding of the material bleed over process and allows for the effect of different surfaces on the transfer ratio to be studied. The materials used in this study were all of the materials that are used in the printing system. Teflon and PDMS are used as printing surfaces due to their nonstick nature. Aluminum is used for the bracket that holds the object as it is being printed. Glass slides may be used to hold cleaning droplets, and the printed parts are made of cured PEGDA 250 resin.

### 3.3.1 Contact angle study

The contact angle of PEGDA 250 on varying surfaces was studied in order to obtain a library of information that could be used to predict liquid bridge behavior between a variety of surfaces.

To measure static, advancing, and receding contact angles of the PEGDA 250 droplet on varying surfaces, the tilting droplet method was used. First, a ~20 μL droplet was placed on the substrate of choice. All materials were washed in distilled water and rinsed in ethanol for 15 minutes before being air dried prior to their use in order to ensure consistent results. A goniometer setup was used with a Canon 60D DSLR camera to take pictures of the droplet profiles. First, a picture of the horizontal droplet was taken so that the static contact angle could be measured. Then, the platform was gradually and gently rotated until the advancing and receding angle of the droplet began to slip. At that instant another picture was taken in order to measure the advancing and receding contact angles. FIGURE 3.2 shows example images taken with a droplet of PEDGA 250 on top of a PDMS substrate.

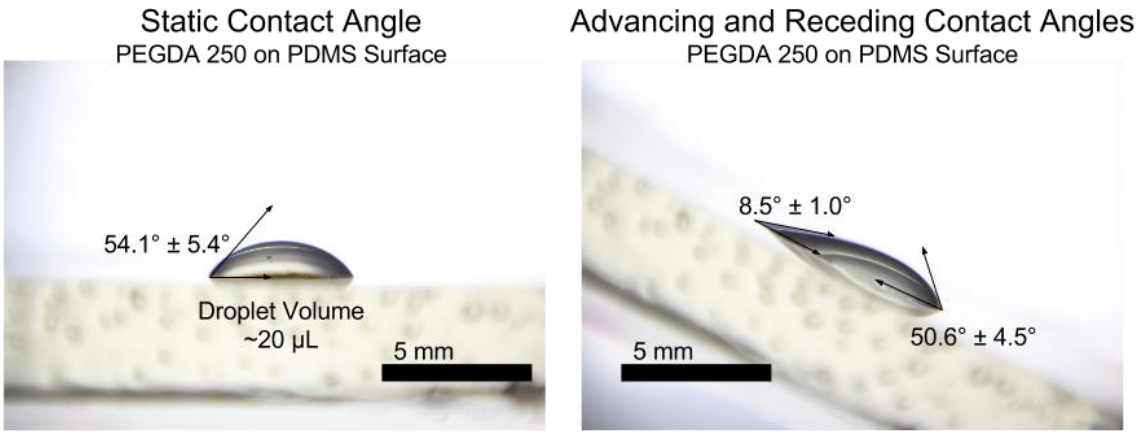


**FIGURE 3.2: Advancing, receding, and static contact angle measurements**

Six different measurements for each material were done, and the final results were averaged and the standard deviation of the measurements was taken. The results are tabulated in TABLE 3.1 and shown graphically in FIGURE 3.3. These results are used later on in order to predict the liquid bridge separation between two different surfaces.

| Material | Static C/A | Receding C/A | Advancing C/A |
|---|---|---|---|
| PEGDA 250 | 22.1° ± 4.6° | 7.3° ± 1.2° | 31.0° ± 5.0° |
| Glass | 34.7° ± 4.0° | 8.1° ± 1.4° | 40.5° ± 4.2° |
| Aluminum | 42.0° ± 5.4° | 9.9° ± 2.0° | 49.5° ± 8.9° |
| PDMS | 54.1° ± 5.4° | 8.5° ± 1.0° | 50.6° ± 4.2° |
| Teflon | 60.7° ± 7.1° | 36.2° ± 5.5° | 75.7° ± 3.4° |

**TABLE 3.1: Advancing, receding, and static contact angles of liquid PEGDA 250 on various surfaces**

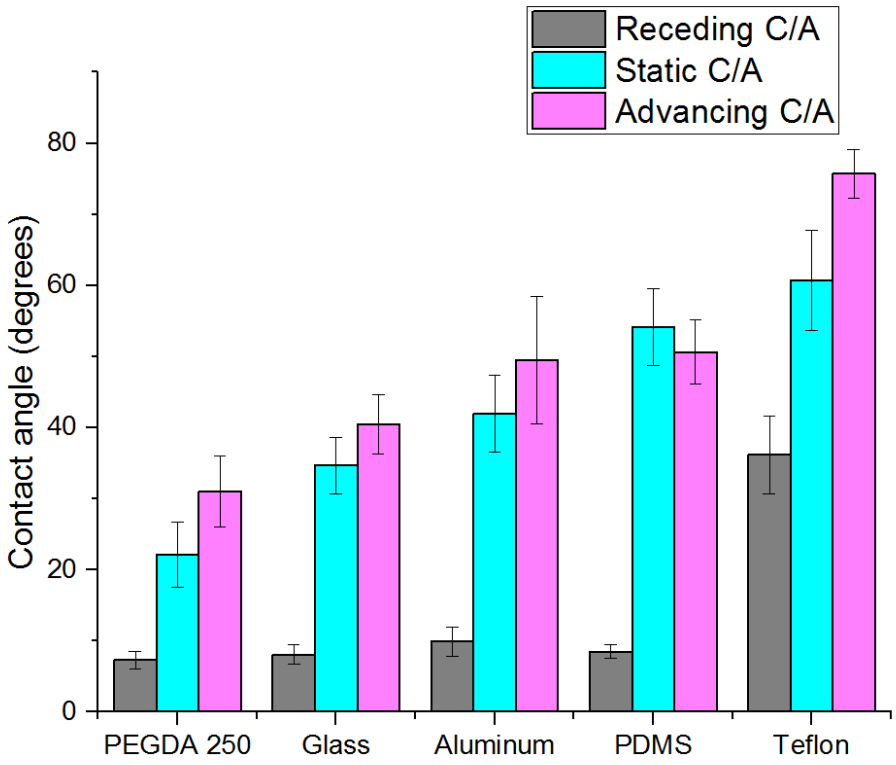


**FIGURE 3.3: Advancing, receding, and static contact angles of liquid PEGDA 250 on various surfaces**

### 3.3.1.1 Theoretical approximation

When studying liquid bridge separation, it must be assured that gravity is not playing a part in the separation of the liquid bridge. The bond number calculates the strength of gravity with respect to surface tension. In order to show that gravity can be neglected for this experiment, the bond number should be less than unity [20]. The bond number is calculated with the following formula.

$$Bo = \frac{gpR^2}{\gamma} \quad [3]$$

In this formula, g is gravitational acceleration, p is the density of PEGDA 250 (1.11 g/mL), R is the characteristic length, in this case the contact radius on the donor surface (the surface on which the droplet originally sits) when the liquid bridge is formed (maximum of 600 μm), and γ is the surface tension of the liquid ($7.28*10^{-2}$ N/m) [19]. The result of this calculation is a bond number of 0.0538, which is less than unity, meaning that the effects of gravity can be neglected for these experiments.

Through numerical fitting of the liquid bridge separation model, H. Chen et al. have come up with a closed-form function that predicts the transfer ratio between two surfaces as solely a function based on the receding contact angles of each surface ($(\theta_r)_{acc}$ on the acceptor (top) surface and $(\theta_r)_{don}$ on the donor (bottom) surface)

$$\alpha_0 = (1+\exp(-3.142((\theta_r)_{acc} + (\theta_R)_{don})^{2.528} * ((\theta_r)_{don} - (\theta_r)_{acc})])^{-1} \quad [4]$$

The transfer ratio is defined as the portion of the liquid droplet that is left on the acceptor surface (top surface in this case) after the liquid bridge breaks. As can be seen, this transfer ratio depends on the magnitude and difference in the receding contact angles of the donor and acceptor surfaces [20]. This equation is in conjunction with the results

from the advancing and receding contact angles on various surfaces is used to predict the various transfer ratios for the liquid bridge study.

#### 3.3.1.2 Breaking liquid bridge study

The liquid bridge breaking study was performed on a goniometer setup like the contact angle study. The surfaces were prepared in the same way as the contact angle study. Each surface was washed in distilled water, rinsed in ethanol for 15 minutes, and air dried before it was used for data collection. The top surface was advanced and receded using a Velmex manual stage that was operated by hand. Video was taken at 60 frames per second using a Canon 60D DSLR. The experiment begins with the placement of a ~120 nL droplet on the bottom surface. The top surface is then lowered until a liquid bridge is formed, and the bottom and top platform are brought close together. Once the platforms are close together, the top platform is solely raised (~10 seconds until breaking) until the liquid bridge separates. The video footage is then analyzed and the frame before the liquid bridge breaks is saved. Using Image J, each half of the liquid bridge is measured, and an approximation of a truncated cone is used to calculate the volume contained in each half of the liquid bridge. These volumes are used to calculate the experimental transfer ratios. Each experiment was performed three times and good agreement between the trials was observed.

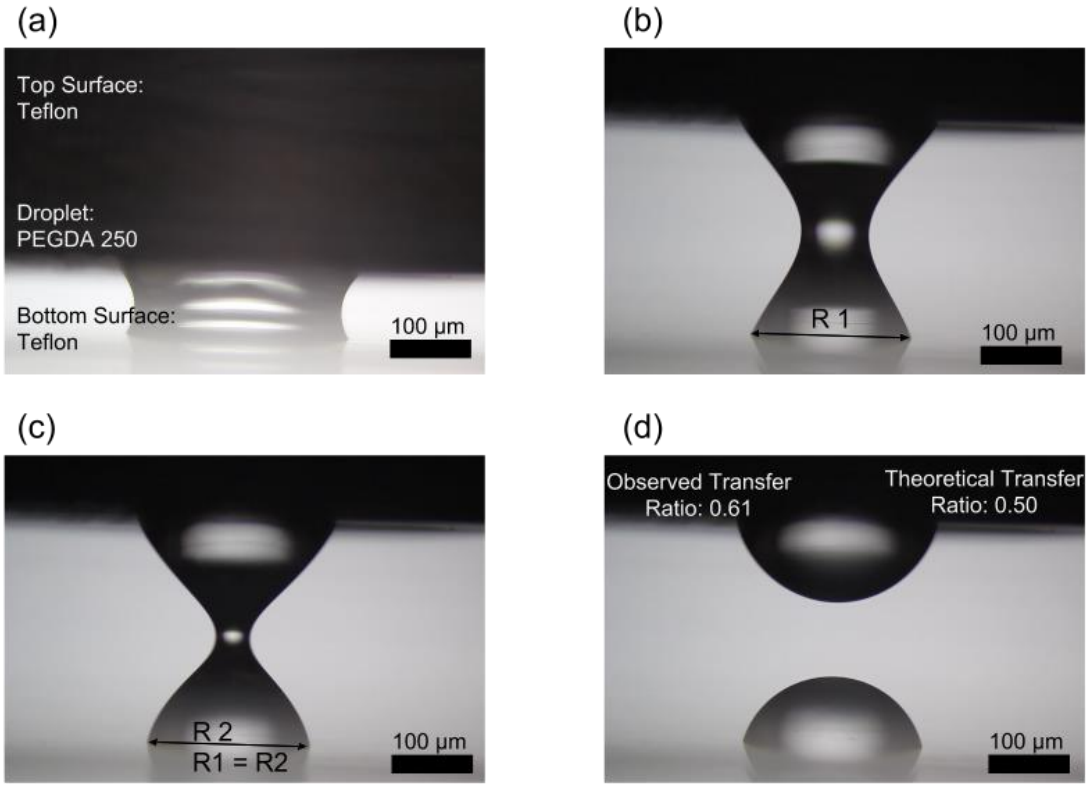


**FIGURE 3.4: Liquid bridge separation with Teflon top and bottom surfaces (a) formation of the liquid bridge (b) the liquid bridge is stretched (c) the last frame before separation (d) separation of the liquid bridge**

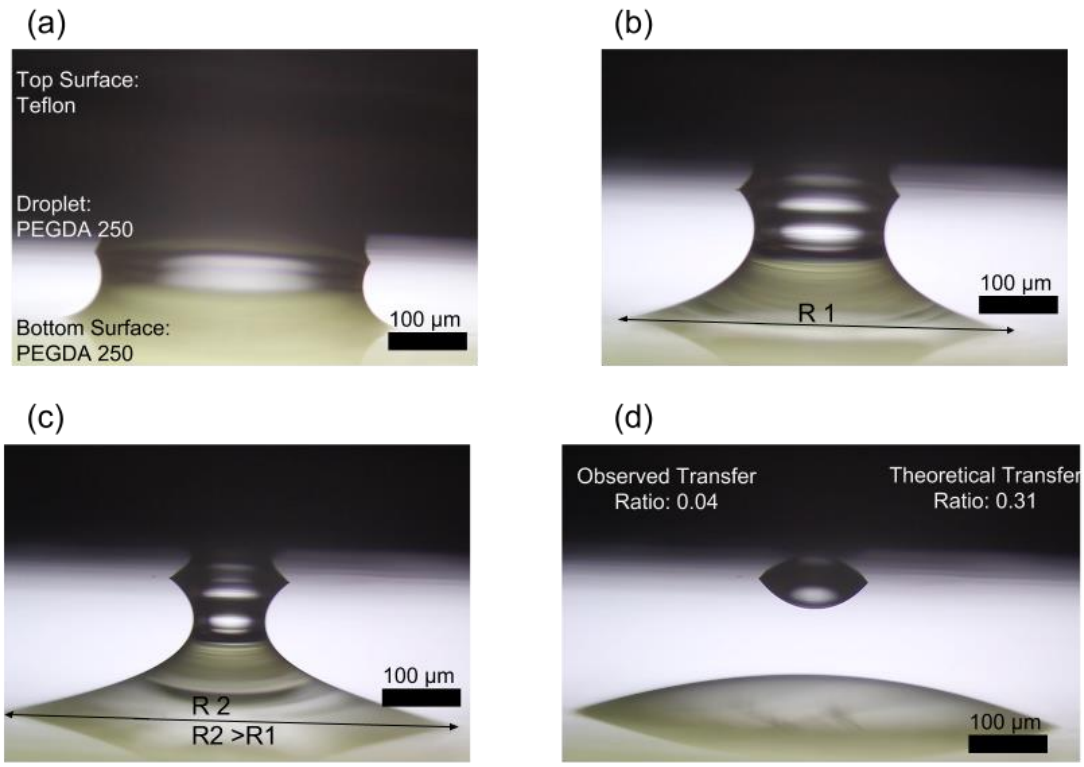


**FIGURE 3.5: Liquid bridge separation with a Teflon top surface and PEGDA 250 bottom surface (a) formation of the liquid bridge (b) the liquid bridge is stretched (c) the last frame before separation (d) separation of the liquid bridge**

FIGURE 3.4 and FIGURE 3.5 show the sequence of a liquid bridge breaking between two Teflon surfaces and a Teflon acceptor surface and a PEGDA 250 donor surface. The results from the experimental measurements and theoretical predictions are tabulated in TABLE 3.2.

| | | BOTTOM SURFACE | | | | |
|---|---|---|---|---|---|---|
| TOP SURFACE | | PEGDA 250 | Glass | Aluminum | PDMS | Teflon |
| PEGDA 250 | measured | .363 ± .030 | .112 ± .006 | .338 ± .010 | .562 ± .022 | .951 ± .002 |
| | theoretical | 0.500 | 0.500 | 0.502 | 0.501 | 0.688 |
| Glass | measured | .335 ± .011 | .350 ± .019 | .296 ± .013 | **.461 ± .012** | .968 ± .004 |
| | theoretical | 0.500 | 0.500 | 0.501 | **0.500** | 0.691 |
| Aluminum | measured | .333 ± .009 | .343 ± .001 | .388 ± .019 | .478 ± .006 | .977 ± .003 |
| | theoretical | 0.498 | 0.499 | 0.500 | 0.499 | 0.697 |
| PDMS | measured | .296 ± .013 | .112 ± .006 | .127 ± .011 | .106± .003 | **.668 ± .020** |
| | theoretical | 0.501 | 0.500 | 0.501 | 0.500 | **0.692** |
| Teflon | measured | .035 ± .003 | .043 ± .003 | .043 ± .006 | .056 ± .001 | **.613 ± .007** |
| | theoretical | 0.312 | 0.309 | 0.303 | 0.308 | **0.500** |

**TABLE 3.2: Liquid bridge separation transfer ratio results**

The data shows similar results in some cases of the transfer ratio measurement, but not all. To understand why this disagreement occurred, the videos of the liquid bridge breakage were analyzed again. The conditions for the model of the liquid bridge breakage model require that the contact angle of the liquid bridge stay constant until the receding contact angle is achieved. At that point, the contact radius slips until the bridge separates. In almost all of the cases, an increasing of the contact line radius was observed as the bridge was about to break, invalidating the model. This increase in contact radius is very clearly seen in FIGURE 3.6. In the second frame, a contact radius of R1 is observed. In the next image, a larger contact radius, R2 is observed. This is contrary to what the model predicts. Three cases were observed to perfectly follow the behavior outlined in the liquid bridge model. These cases are bolded in TABLE 3.2. For all of these results, the theoretical and observed transfer ratios are very close, and much closer to the theoretical results than the other trials which do not follow the liquid bridge model. All of the results for transfer ratio between two different surfaces are shown graphically in FIGURES 3.6 – 3.10.

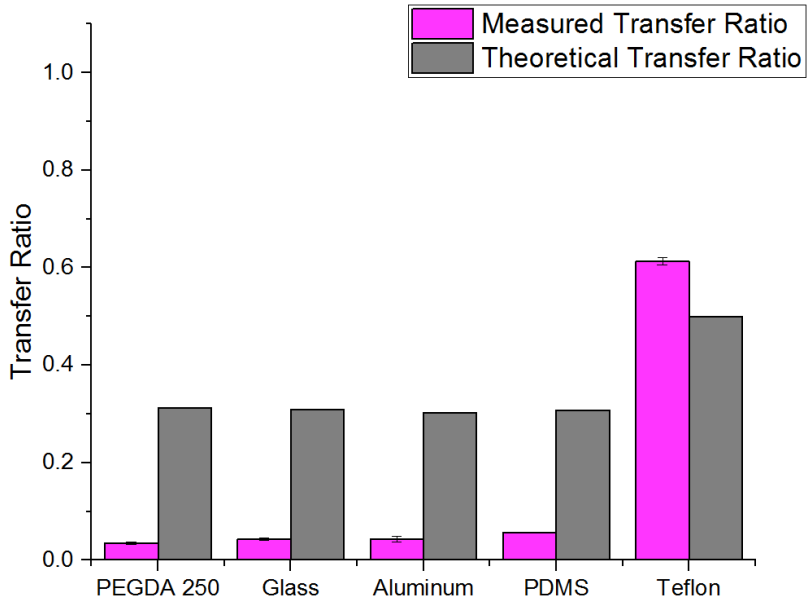


**FIGURE 3.6: Teflon top surface, liquid bridge separation transfer ratios**

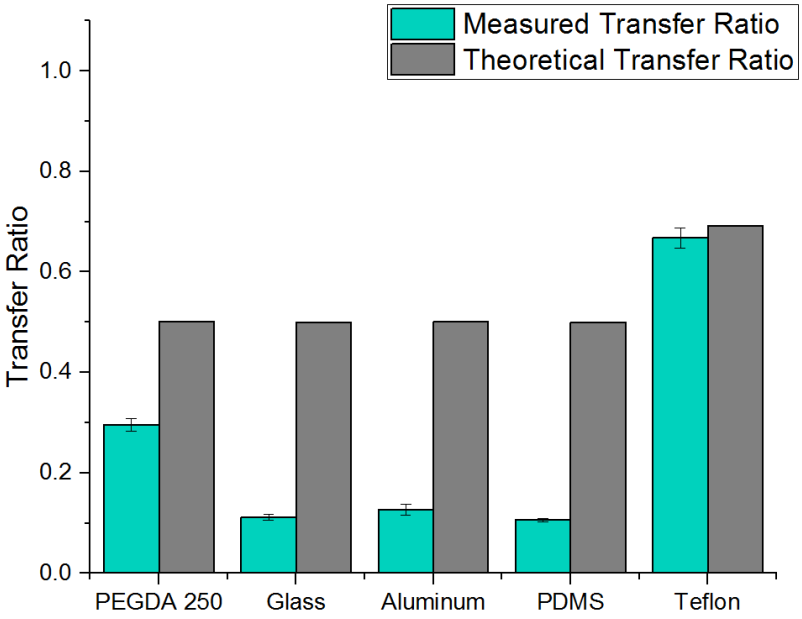


**FIGURE 3.7: PDMS top surface, liquid bridge separation transfer ratios**

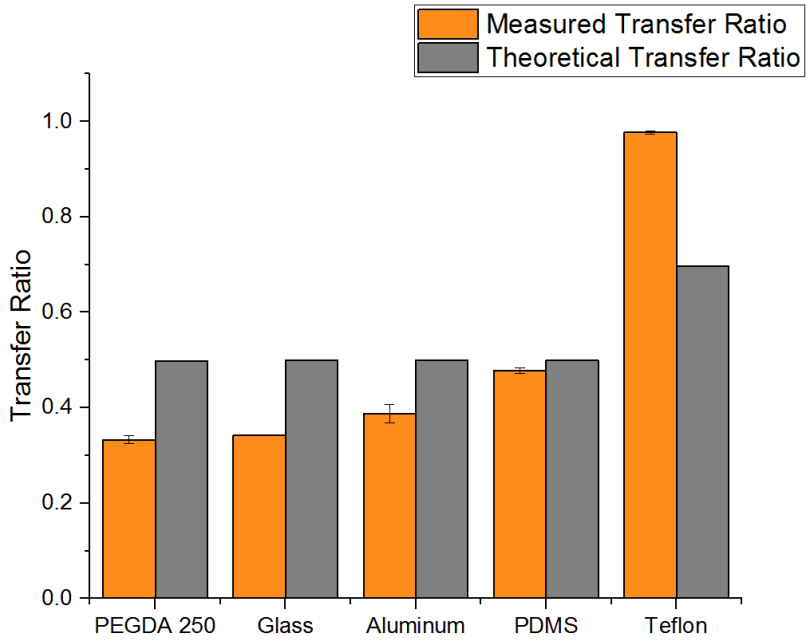


**FIGURE 3.8: Aluminum top surface, liquid bridge separation transfer ratios**

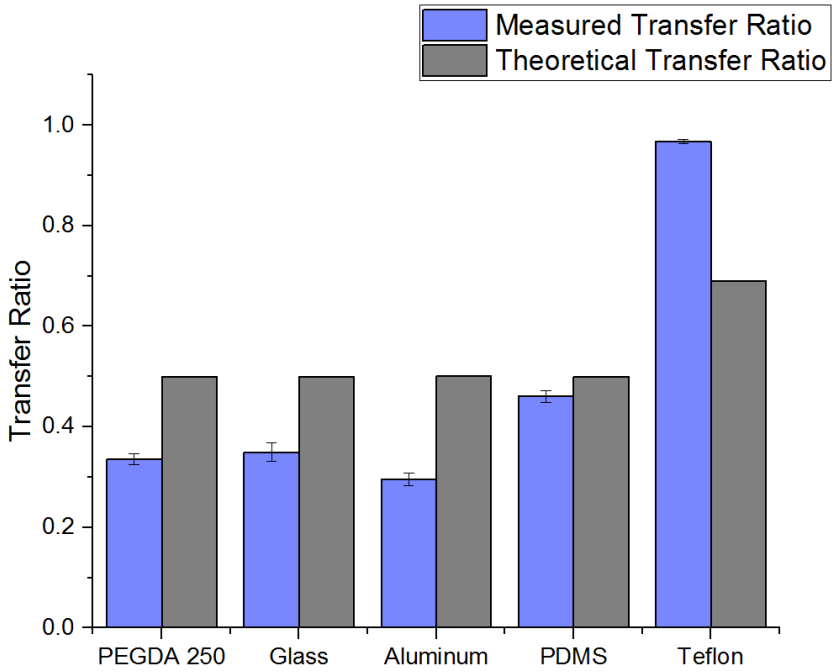


**FIGURE 3.9: Glass top surface, liquid bridge separation transfer ratios**

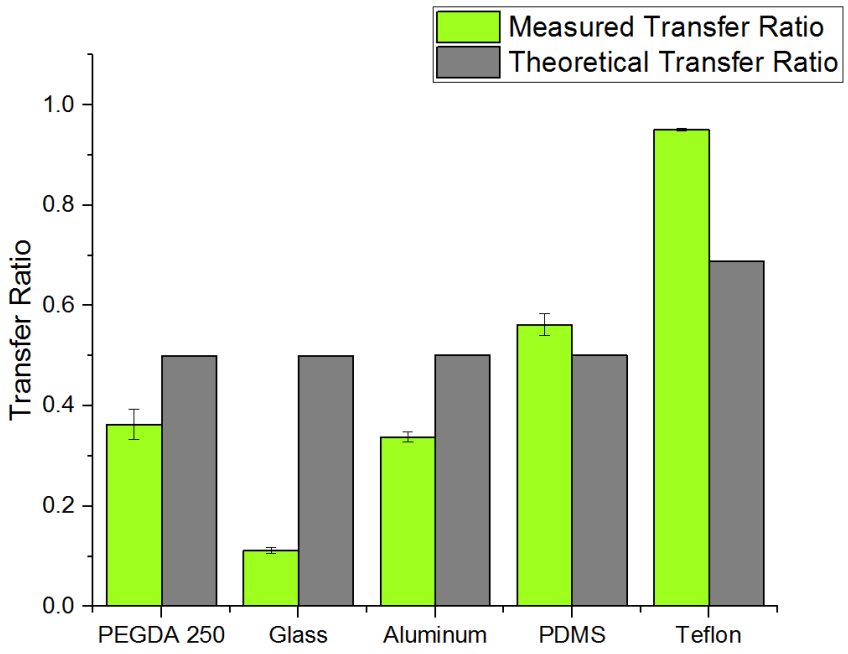


**FIGURE 3.10: PEGDA 250 top surface, liquid bridge separation transfer ratios**

### 3.4 Transfer ratio of droplet in the 3D printing system

While liquid bridge studies between two flat surfaces are helpful to understand how liquid bridge transfer works between two surfaces, this is not how the separation f resin in the system will actually occur during the printing process. During the printing process, a printed structure will also be attached to the top platform and will influence the transfer ratio of the resin droplets and the cleaning droplets. In order to mimic various structures, three cylinders were printed. Each cylinder has ten layers and a total height of 1mm. The diameters of the three cylinders were 1.56 mm (200 pixels), 3.12 mm (400 pixels), and 4.56 mm (600 pixels). For each trial, a ~6 μL droplet of PEGDA 250 or ethanol was placed on the PDMS surface. The, the top platform was lowered until the structure came

into contact with the PDMS layer. Then, the top surface was raised, forming a liquid bridge. As the platform raises, the liquid bridge will stretch and finally break. After breaking, the volume of the droplet on the bottom surface was measured and compared with the original droplet volume in order to calculate the transfer ratio. The sequence is shown in FIGURE 3.11.

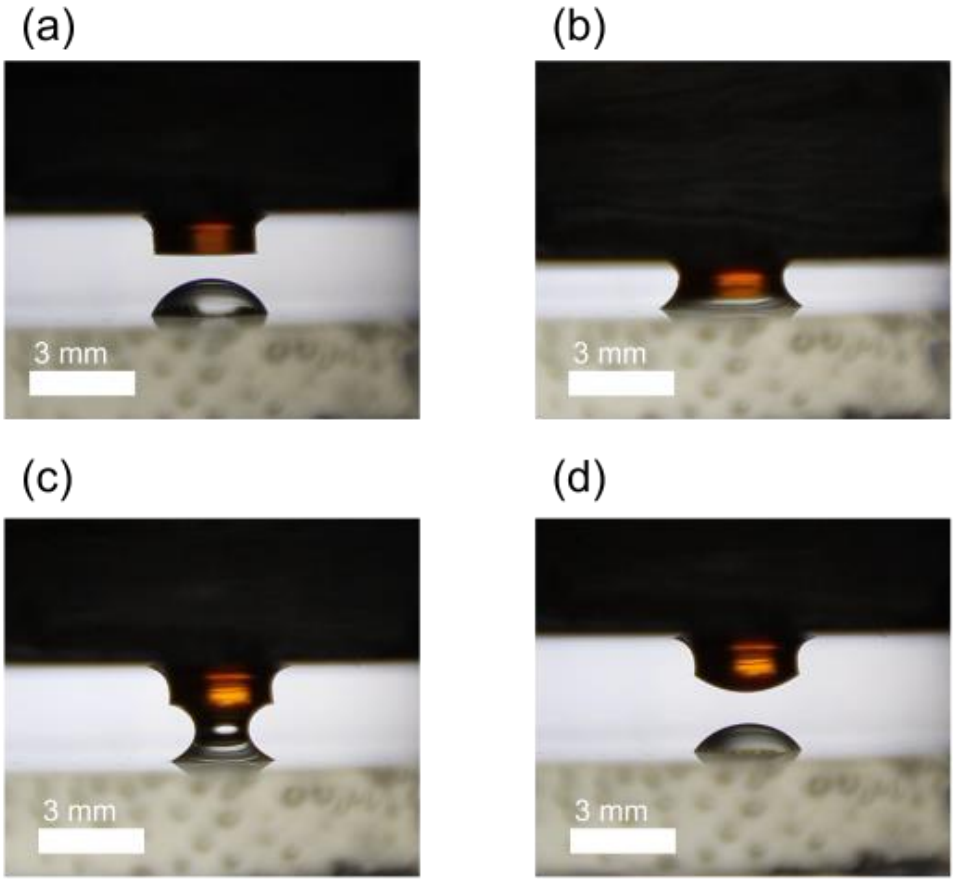


**FIGURE 3.11 Process for transfer ratio study with printed structures (a) droplet is placed on PDMS surface (b) cylinder is fully lowered on the droplet (c) stage is raised again and liquid bridge stretches (d) liquid bridge breaks and transfer ratio is measured**

The results for the system separation test are shown in TABLE 3.3 and FIGURE 3.12. The general trend shows that the larger the cylinder is, the higher the transfer ratio will be, for both PEGDA 250 and ethanol droplets. This trend is expected as a larger diameter has a larger surface if the height is held constant. This larger surface will hold on the liquid droplet better, increasing the transfer ratio.

| | **Transfer Ratio PEGDA 250** | **Transfer Ratio Ethanol** |
|---|---|---|
| **1.56mm cylinder** | .312±.017 | .304±.098 |
| **3.12mm cylinder** | .357±.045 | .497±.095 |
| **4.56mm cylinder** | .515±.040 | .541±.069 |

**TABLE 3.3 Transfer ratio results for different diameters of cylinders**

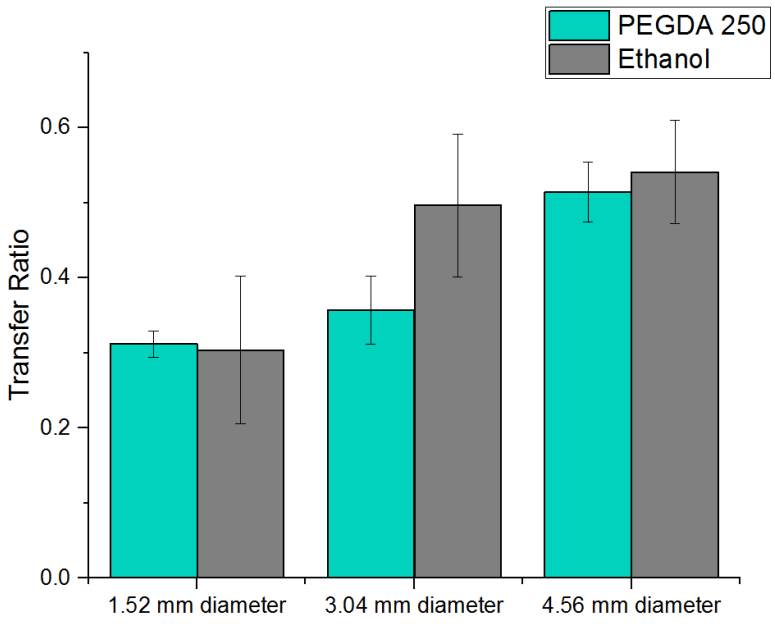


**FIGURE 3.12 Transfer ratio results for different diameters of cylinders**

## 3.5 Electrowetting

The goal of the application of electrowetting in the droplet based multi-material printing system is to provide a nonstick printing surface when no voltage is applied, and to attract the remaining resin to the build platform when voltage is applied as the Z axis recedes. This reversible wetting should provide a nonstick surface to print on while reducing resin left on the part, and therefore material bleed over.

### 3.5.1 Resin conductivity

In order for electro-wetting to work, the resin droplet must be able to conduct electricity. The resin used for these tests was PEGDA 250. An organic salt, imidazole trifluoromethanesulfonate sale (henceforth referred to as ITFMS, Sigma-Aldrich, St. Louis, MO) was added to the PEGDA 250 to allow the originally nonconductive resin to conduct electricity. FIGURE 3.13 shows the effect of the concentration of the ITFMS salt on the conductivity of PEGDA 250. With no concentration of ITFMS salt, the resistance of the PEGDA 250 across a distance of 1.32 inches was > 40Mohms. The resistance of the PEGDA 250 across the 1.32 inch distance decreased significantly with the addition of ITMFS salt. An adequately low resistance was obtained with the addition of 5% by weight ITFMS salt to PEGDA 250, so this concentration was chosen as the standard for the remaining experiments.

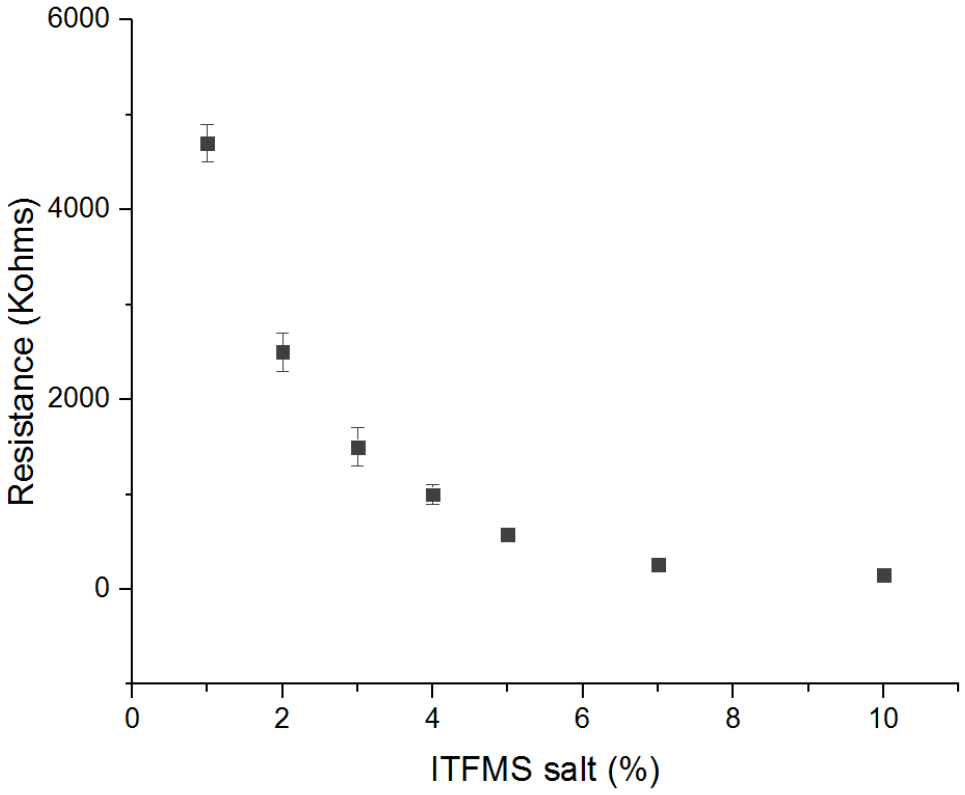


**FIGURE 3.13: Conductivity of PEGDA 250 versus Concentration of ITFMS Salt**

### 3.5.2 Electrowetting with electrode

To study the effect of electrowetting, the most simple electrowetting setup was tested first. The contact angle of the liquid droplet on the printing surface as voltage is applied will follow the Young-Lipmann curve.

$$\cos(\theta_v) = \cos(\theta_0) = \frac{1}{2} * \frac{\varepsilon\varepsilon_0}{\gamma_{lv}t} V^2 \qquad [5]$$

Where $\theta_0$ is the contact angle without applied potential, $\theta_v$ is the contact angle when a specified voltage is applied, $\varepsilon$ is the dielectric constant of the insulating layer (15μm thick PDMS coating on an ITO coated glass slide), $\varepsilon_o$ is the dielectric constant of air, t is the

thickness of the PDMS layer, $\gamma_{lv}$ is the surface tension at the liquid-vapor interface, and V is the applied voltage [22].

In this experiment, voltage is supplied via a EMCO high voltage proportional power supply fed by a generic benchtop lab DC power supply. The electrode that touches the droplet is a 26 gauge bare wire. The surface upon which the droplet sits is a ~15μm thick PDMS layer coated on ITO coated glass slide. The PDMS, Dow Corning, Midland, MI was spun coated on top of the 1mm thick ITO coated glass slide (Adafruit, New York, NY) using a spin coater. The PDMS was prepared in a 10:1 radio and degassed in a vacuum chamber. The coating was spun by ramping up to 4500 RPM and holding that speed for 45 seconds before decelerating, giving a final coating thickness of ~15μm. The negative terminal of the power supply is connected to the ITO coated on the glass slide. The experimental setup is shown in FIGURE 3.14. Care was taken to make sure that the vibration isolation table was isolated from the high voltage being used in the experiment.

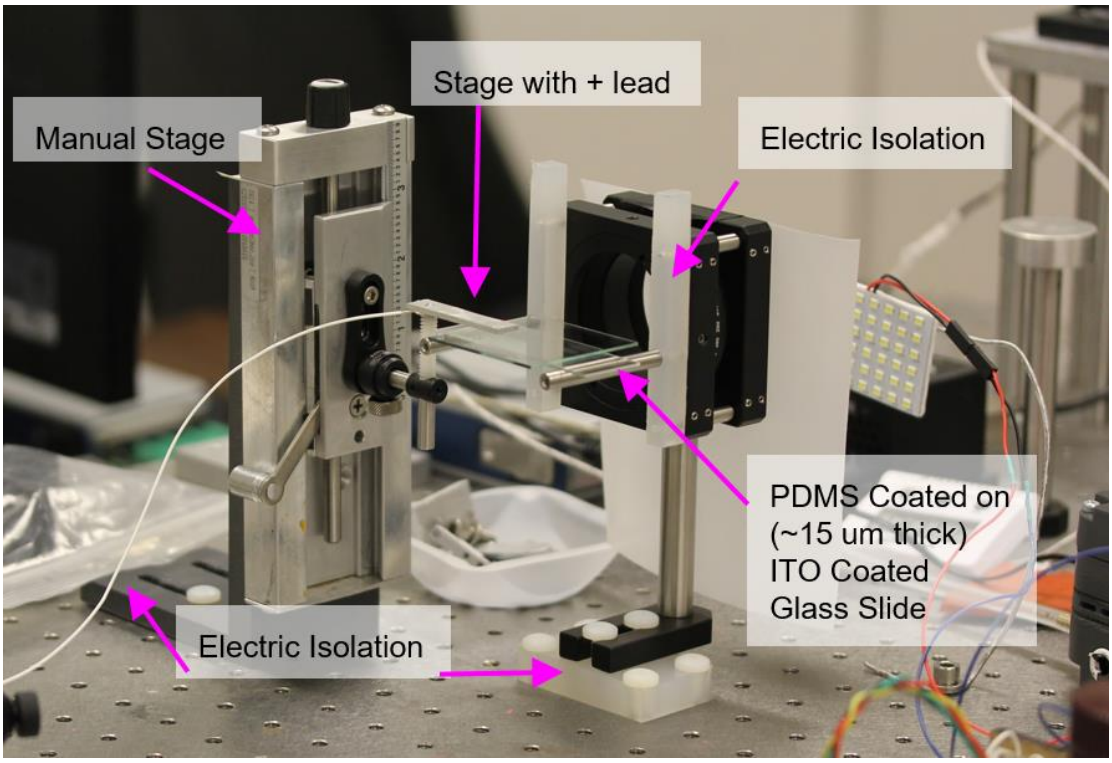


**FIGURE 3.14: Experimental setup for the electrowetting tests**

The experiment was conducted by lowering the wire into the droplet of tap water or conductive PEGDA 250 and then adjusting the voltage of the power supply. The droplet size for the tap water trial and the PEGDA trials was ~20 µL. Contact angles on both sides of the droplet were measured and averaged for each data point. The voltage was adjusted from 0V to the point of dielectric breakdown, which was typically 250V. FIGURE 3.15 shows the experimental result of the droplet contact angles for the minimum and maximum voltages applied to the droplet.

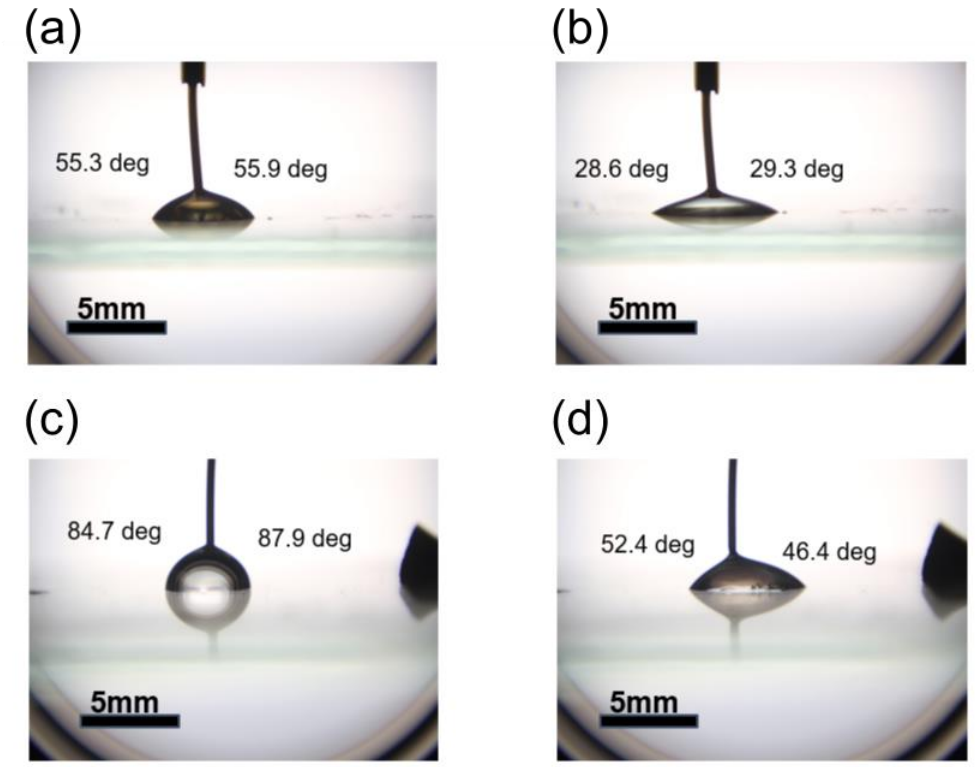


**FIGURE 3.15: Electrowetting of PEGDA 250 and tap water on PDMS and ITO coated glass (a) PEGDA 250 at 0V (b) PEGDA 250 at 250-267V (c) tap water at 0V (d) tap water at 225V**

The tap water results stop at ~225V due to the breakdown of the PDMS coating, and the PEGDA 250 droplet reached a maximum of ~267V. The averaged contact angle results were plotted versus the applied voltage along with the theoretical Young-Lipmann curve. This plot is shown in FIGURE 3.16. The results follow the theoretical Young-Lipmann curve closely. The tap water results diverge from the theoretical Young-Lipmann curve around 150V. This divergence is expected and is due to contact angle saturation. At the contact angle saturation point, even though voltage can be increased and the Young-Lipmann curve predicts that the contact angle will continue to decrease, it will not.

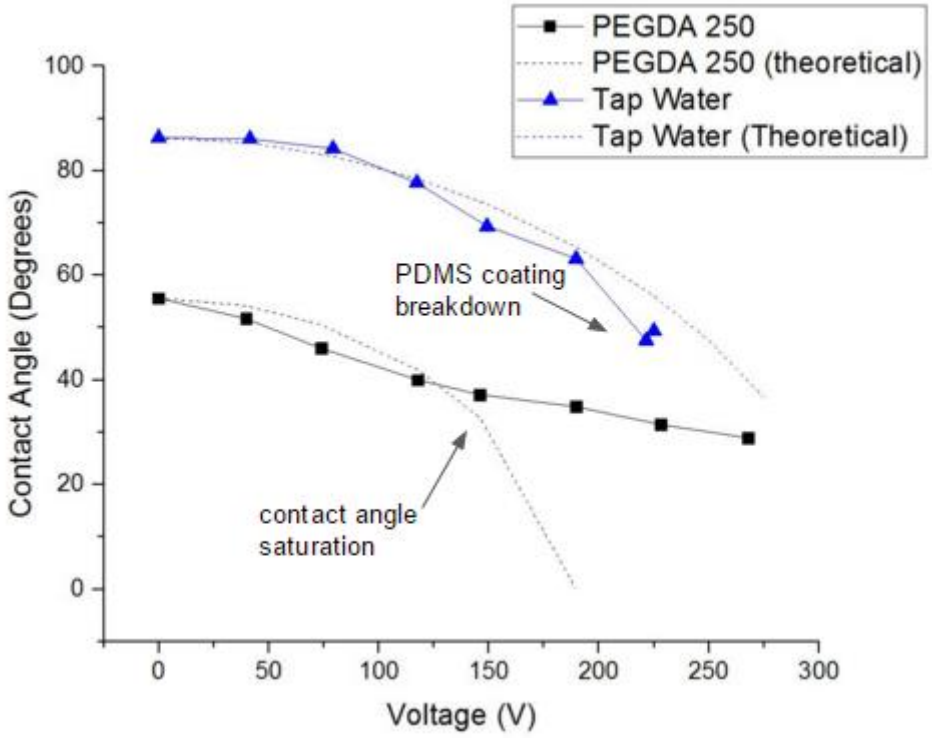


**FIGURE 3.16: Contact angles of PEGDA 250 and tap water compared to theoretical Young-Lipmann curve**

For tap water and PEGDA 250, the static contact angle was reduced by approximately ½ using electrowetting. This decrease in contact angle should have an effect on the liquid bridge transfer, and will decrease the transfer ratio during liquid bridge separation, reducing material bleed over.

# 4 Conclusions and Future Directions

A droplet-based multi-material 3D printer has significant benefits compared to competing systems. The system is able to create fine features (~114 μm) and multiple material prints with minimal bleed over all the way down to feature sizes of ~190 μm. Not only can the system produce finer parts in less time than competing "rotating vat" systems, but it also requires less material and is over 50 times more material efficient than "fillable chamber" type multiple material 3D printers.

The droplet-based multiple-material printing system has many benefits over competing systems, and there is still room for improvement. In order to reduce the amount of bleed over so that multiple materials can be used all the way to the resolution limit of the 3D printer, electrowetting can be used. By studying the contact angle of the resin on varying surfaces, and the liquid bridge separation between different surfaces, it has been shown that a decrease in receding contact angle on the bottom printing surface will reduce transfer ratio of the liquid bridge.

Electrowetting has been shown to reduce the contact angle of the PEGDA 250 resin on the PDMS coated printing surface. This reduction in contact angle must be proven to correlate to a decrease in receding contact angle. A reduction of the receding contact angle of the PEGDA 250 on the printing surface will reduce the transfer ratio of the resin and reduce material bleed over.

A material efficient and high resolution multiple material 3D printer has many potential uses in various fields. Biological fields will appreciate the material savings when using expensive materials to build cell scaffolds or other fins structures. Also the robustness of the system allows for materials to be printed that are otherwise unable to be printed. Suspensions of particles or highly viscous materials that are normally incompatible with competing 3D printing systems can be printed without difficulty with the droplet-based multiple-material 3D printer. The creation of a 3D printing system that can use a wide variety of materials, prints in a time efficient manner, can resolve fine features, and wastes little material is a true advancement in the current state of the art of 3D printing.

**References**

[1] http://www.designboom.com/technology/3d-printed-houses-in-24-hours-04-24-2014/

[2] http://www.stratasys.com/3d-printers/design-series/dimension-elite

[3] Gibson, I., D. W. Rosen, and B. Stucker. Additive Manufacturing Technologies: Rapid Prototyping to Direct Digital Manufacturing. New York: Springer, 2010. Print.

[4] http://www.nanoscribe.de/files/5014/2062/6360/Flyer_PPGT_web.pdf

[5] D. Espalin, J. Ramirez, F. Medina, and R. Wicker, "Multi-material, multi-technology FDM: exploring build process variations," *Rapid Prototyping Journal,* vol. 20, no. 3, pp. 236-244, 2014.

[6] http://store.makerbot.com/replicator2x

[7] B. Derby, "Printing and Prototyping of Tissues and Scaffolds," *Science,* vol. 338, pp. 921-926, Nov. 2012.

[8] D. Kolesky, R. Truby, S. Gladman, T. Busbee, K. Homan, and J. Lewis, "3D Bioprinting of Vascularized, Heterogeneous Cell-Laden Tissue Constructs," *Adv. Mater.*, vol. 25, pp. 3124-3130, 2013.

[9] A. Gladman, E. Matsumoto, R. Nuzzo, L. Mahadevan, and J. Lewis, "Biomimetic 4D printing," *Nature Materials*, advance online publication, 2016.

[10] http://www.stratasys.com/3d-printers/design-series/objet30-pro

[11] S. Ready, G. Whiting, and T. Nga Ng, "Multi-Material 3D Printing," *Society for Imaging Science and Technology, Digital Fabrication and Digital Printing: NIP30 Technical Program and Proceedings*, pp. 121-123, 2014.

[12] C. Sun, N. Fang, D.M. Wu, and X. Zhang, "Projection micro-stereolithography using digital micro-mirror dynamic mask," *Sensors and Acruators,* vol. 121, pp. 113-120, 2005.

[13] X. Zheng, J. Deotte, M. Alonso, G. Farquar, T. Weisgraber, S. Gemberling, H. Lee, N. Fang, and C. Spadaccini, "Design and optimization of a light-emitting diode projection micro-stereolithography three-dimensional manufacturing system," *Review of Scientific Instruments*, vol. 83, 125001, 2012.

[14] Y. Myound Ha, J. Won Choi, and S. Hee Lee, "Mass production of 3-D microstructures using projection microstereolithography," *Journal of Mechanical Science and Technology,* vol. 22, pp. 514-521, 2008.

[15] J. Choi. H, Kim, and R. Wicker, "Multi-material stereolithography," *Journal of Materials Processing Technology*, vol. 211, pp. 318-328, 2011.

[16] C. Zhou, Y. Chen, Z. Yang, and B. Khoshnevis, "Digital material fabrication using mask-image-projection-based stereolithography," *Rapid Prototyping Journal*, vol. 19, pp. 153-165, 2013.

[17] J. Choi. E. MacDonald, and R. Wicker, "Multi-material microstereolithography," *International Journal of Advanced Manufacturing Technology*, vol. 49, pp. 543-551, 2009.

[18] H. Chen, A. Amirfazli, and T. Tang, "Modeling Liquid Bridge between Surfaces with Contact Angle Hysteresis," *Langmuir*, vol. 29, pp. 3310-3319, 2013.

[19] H. Chen, A. Amirfazli, and T. Tang, "Liquid transfer mechanism between two surfaces and the role of contact angles," *Soft Matter*, vol. 10, pp. 2503-2507, 2014.

[20] H. Chen, T. Tang, and A. Amirfazli, "Effects of surface wettability on fast liquid transfer," *Physics of Fluids*, vol. 27, 112102, 2015.

[21] F. Mugele, and J. Baret, "Electrowetting: from basics to applications," *Journal of Physics: Condensed Matter*, vol. 17, pp. 705-774, 2005.

[22] F. Saeki, J. Baum, H. Moon, J. Yoon, C. Kim, and R. Garrell, "Electrowetting on Dielectrics (EWOD): Reducing Voltage Requirements for Mircofluidics,"

[23] J. Hopkins, Y. Song, H. Lee, N. Fang, and C. Spadaccini, "Polytope Sector-Based Synthesis and Analysis of Microstructural Architectures With Tunable Thermal Conductivity and Expansion," *Journal of Mechanical Design*, vol. 138, pp. 151401-1-10, 2016.